MULTIFUNCTIONAL PIEZOELECTRIC METASTRUCTURES FOR VIBRATION ATTENUATION AND ENERGY HARVESTING

A Dissertation
Presented to
The Academic Faculty

By

Mohid Muneeb Khattak

In Partial Fulfillment
of the Requirements for the Degree
Master of Science in the
G.W. Woodruff School of Mechanical Engineering

Georgia Institute of Technology

May 2021

© Mohid Muneeb Khattak 2021

MULTIFUNCTIONAL PIEZOELECTRIC METASTRUCTURES FOR VIBRATION ATTENUATION AND ENERGY HARVESTING

Thesis committee:

Dr. Alper Erturk, Advisor
School of Mechanical Engineering
Georgia Institute of Technology

Dr. Aldo A. Ferri
School of Mechanical Engineering
Georgia Institute of Technology

Dr. Julien Meaud
School of Mechanical Engineering
Georgia Institute of Technology

Date approved: April 16, 2021

The world is a book and those who do not travel read only one page.

St. Augustine

For my Amma, without her prayers all this would not have been possible.

ACKNOWLEDGMENTS

I would like to start off by thanking my advisor Professor Dr. Alper Erturk, who has not only been a teacher to me, but also a mentor. I am grateful to him for providing me the opportunity to work in the Smart Structures and Dynamical Systems Lab (SSDSL). He has provided me with support whenever needed, and has always been there to troubleshoot my problems and provide me with valuable insight throughout the course of my research. He has always given me a flexible atmosphere to work where I am comfortable and for all that, I am obliged.

I would also like to extend a hand of gratitude towards my fellow colleagues at SSDSL especially Dr. Christopher Sugino and Dr. Yiwei Xia who have helped me conduct experiments and provide all sorts of technical expertise I required. They also made sure to impart every bit of knowledge to me whenever I needed it without any hesitation, and have been my greatest source of information till the time I was at SSDSL.

Additionally, I am thankful to Dr. Aldo Ferri and Dr. Julien Meaud for taking out the time and serving as members on my thesis committee. Their feedback intrigued me to think about my research from a different perspective and its further future prospects.

Lastly, I am grateful to my family and friends for being there with me in this roller coaster of a year. Special mention for my Pakistani family here who tolerated me in Atlanta for two years. I am thankful for all the gatherings we had and all the FIFA sessions that helped me remain sane. Finally, I am extremely obliged to the Fulbright Program, without their funding and support I would not have been here.

TABLE OF CONTENTS

LIST OF TABLES

LIST OF FIGURES

LIST OF ACRONYMS

FRF frequency response function

LDV laser Doppler vibrometer

LR locally resonant

OC open circuit

PEH piezoelectric energy harvesting

PZT Lead Zirconate Titanate

RL resistor-inductor

SC short circuit

VEH vibrational energy harvesting

SUMMARY

Over the past two decades, there has been a substantial increase in research conducted on energy harvesting techniques. With the developments in low-power electronic devices and sensors, such as wearable electronics and wireless sensors used in structural health monitoring, energy harvesting is expected to become a viable solution to overcome the need for battery replacement or recharging as well as relevant maintenance efforts. Among the different methods of energy harvesting, vibrational energy is readily available in various forms spanning from human motion to seismic activities. This thesis explores an interesting opportunity to research multifunctional vibrational energy harvesting (VEH). In most applications, vibrations are unwanted and may result in damage or failure of structures. This opens up a pathway to research into VEH techniques which simultaneously can harness useful energy and attenuate these harmful vibrations. Locally resonant LR metastructures are metamaterial-based finite structures with engineered properties that exhibit local resonance. Bandgap formation is a dynamic property exhibited by these LR metastructures where, for a range of frequencies, wave propagation is forbidden (and this bandgap can be tuned for wavelengths larger than the lattice size). This thesis discusses multifunctionality of these structures for concurrent vibration mitigation and low-power energy harvesting. Specifically, the work detailed in this thesis focuses on piezoelectric energy harvesting utilizing the inherent property of piezoelectric elements for converting mechanical strain into electrical energy. Electromechanical models are developed and analyzed numerically for various LR vibrating structures including linear and non-linear cantilever beams. LR metastructures made from (1) linear mechanical resonators with piezoelectric elements, (2) linear electromechanical (piezoelectric) resonators with resistive inductive shunts, and (3) bistable attachments with piezoelectric elements are explored both experimentally and numerically. Conclusions are drawn based on the results obtained in this work.

CHAPTER 1
INTRODUCTION AND BACKGROUND

1.1 Vibrational Energy Harvesting

Energy harvesting (or scavenging) is the process whereby energy is obtained from various sources, and stored in a use-able form to be employed for a variety of applications. Some of these sources include but are not limited to mechanical, solar, thermal, etc. which are utilized using respective transducers such as photovoltaics [1–4], thermoelectrics [5–7] or electromechanical transducers [8–11]. The limited life-time and periodic recharging requirement has been a persistent issue in portable low-powered devices. A solution would be to transition towards something which could serve as an alternative to conventional power sources. Researchers have been working to solve this dilemma ever more efficiently especially in the past two decades. Among the sources of energy harvesting, vibrational energy is the most beneficial since it is very common not only in the natural environment but also due to practical operations such as in the case of rotatory machines. This can be utilized to a greater potential once the environmental effects are decoupled from such harvesting systems.

Vibrational energy harvesting (VEH) is a concept wherein ambient vibrational energy is utilized to generate electricity to power small electronic components [12, 13]. This technique can replace or supplement conventional batteries, reducing the costs associated with accessing and replacing or recharging batteries for remote sensors. A typical vibrational energy harvesting mechanism is shown in Figure 1.1 which includes an external energy source of ambient vibrational energy, a transducer to convert energy from external energy to electric power, a harvesting circuit to optimize the harvesting efficiency and a storage battery or a load circuit.

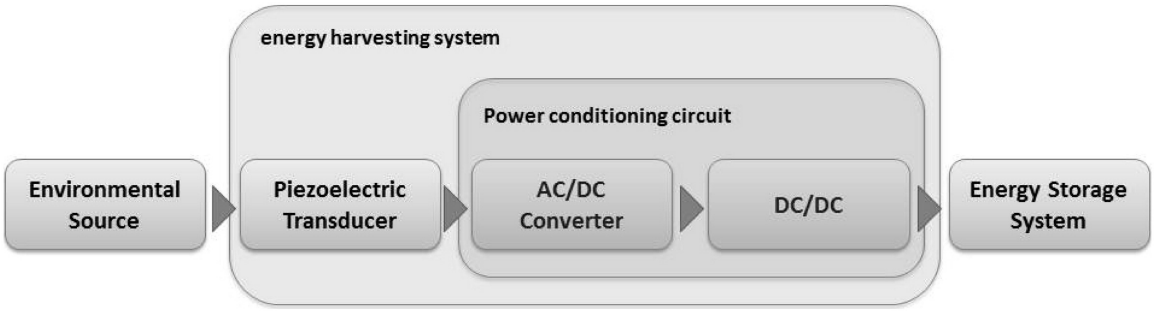

Figure 1.1: An energy harvesting system process [14]

1.2 Piezoelectric Energy Harvesting

The direct piezoelectric effect refers to a phenomenon which converts mechanical strain into electricity. Piezoelectric energy harvesting (PEH) [15–17] is a technique which uses this effect to harness vibrational energy from human motion, seismic activities, etc. and converts it into usable voltage output. This fundamental behavior of piezoelectric materials emerges from their constitutive property and does not require the use of an external voltage input. Piezoelectric materials also have a high power density and they grant an ease of application due to which they are preferred over other conventional vibration energy conversion mechanisms such as electromagnetic [18, 19] and electrostatic [20, 21] techniques. Adding to that, since piezoelectric energy harvesters rely on ambient vibrations which are readily available due to operating conditions of a system, they are much more advantageous than other harvesting technologies reliant upon purely unpredictable environmental conditions.

Since most piezoelectric harvesting systems generate power on the order of micro to milliwatts, it is an obvious choice to use them for applications involving low-power electronics like biomedical devices or portable electronics. Delving into the ease of application as an added utility, piezoelectric harvesting devices are straightforward to manufacture in a multitude of configurations [22–24], including micro-scale concepts and devices [25]. This is represented by Figure 1.2. As this field continues to grow, researchers have introduced VEH capabilities to numerous types of vibrating structures [17, 26], such as linear

cantilevers, bistable beams [24, 27] and plates [28], among others.

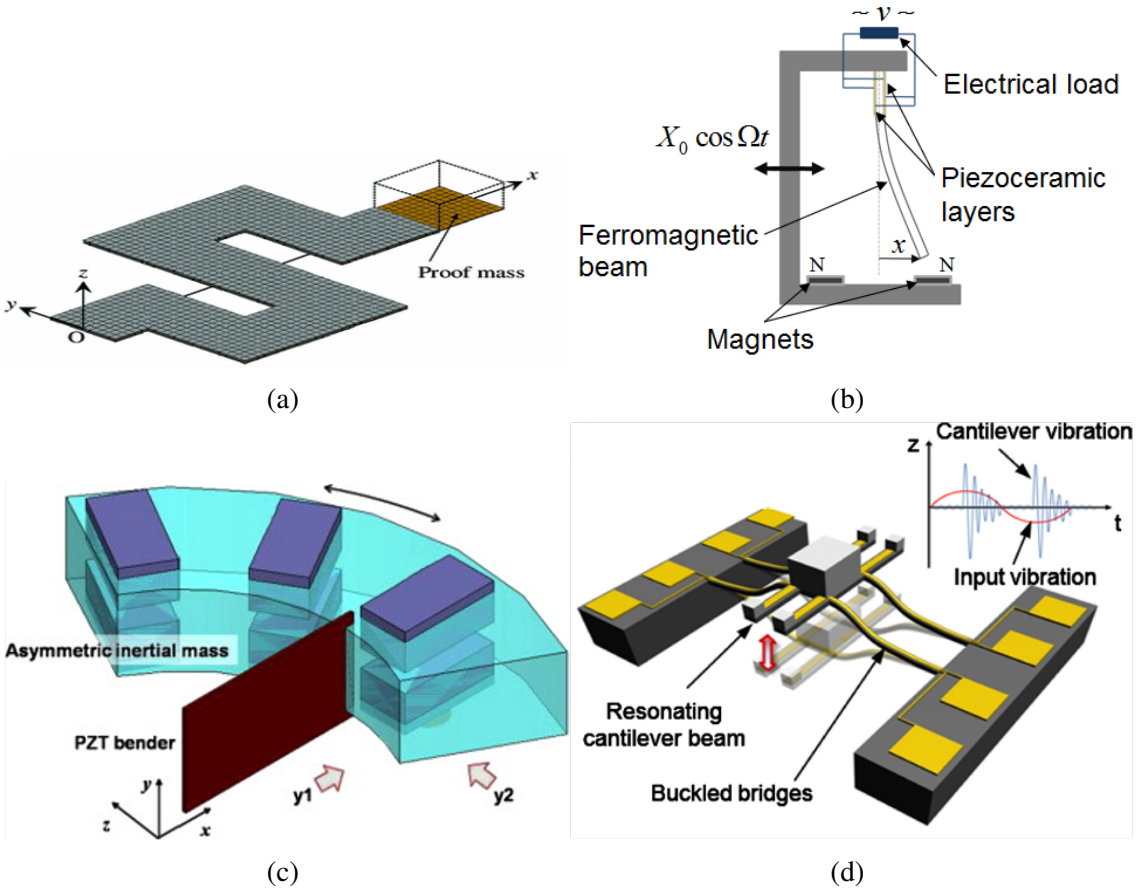

Figure 1.2: (a) S-shaped harvester configuration [29]. (b) Bistable piezomagnetoelastic energy harvester [30]. (c) Energy harvester manufactured with asymmetry [31]. (d) Resonating cantilever beam on a buckled bridge [32].

1.3 Metamaterials and Metastructures

Metamaterials are materials that exhibit properties which are not readily found in ordinary materials, such as a negative refractive index and negative dynamic mass, as shown in Figure 1.3. Metamaterial-based finite structures with specified boundary conditions are called metastructures, and they retain the desired metamaterial phenomena in a finite structural setting. Locally resonant (LR) metastructures exhibit unit cell resonance as a result of the composite inclusions of the material they are made of [33]. This local resonance results in a long wavelength bandgap formation (a bandgap is a range of frequencies where a wave

cannot propagate). LR metastructures [26, 34] enable the ability to form a bandgap at wavelengths much larger than the lattice size as opposed to bandgaps obtained via Bragg scattering. Therefore, LR bandgap is essential for vibration attenuation and respective applications at low frequencies.

1.4 Vibration Attenuation

So far only the benefits of vibrations have been discussed in the context of energy harvesting. Vibrational energy can be harmful as well if not contained in some way. It is a natural physical phenomenon which can be disastrous not only for civil structures but mechanical equipment as well. This calls for solutions that aim towards controlling and mitigating such harmful vibrations before they cause fatigue failure [37] in structures. For this reason, dynamic vibration absorbers are used which are like secondary masses attached to the primary mass in order to absorb and dissipate vibrations from the main structure [38–40].

Conventional mechanical damping techniques for vibration attenuation make use of added masses to act as resonators in order to absorb harmful vibrations. Orthodox means of developing mechanical resonators bring forth complexities if structural vibration attenuation is to take place on structures which are flexible and light-weight. In order to tackle this dilemma, researchers have been studying about and incorporating shunt damping as an effective alternative to conventional means [41, 42]. Conversion of mechanical stress to electrical signals using piezoelectricty allows for easier manipulation and autonomy in design using all the varying methods available in the electrical domain. Examples include passive vibration control using electromechanical shunt damping by Behrens et al. [43], or piezoelectric shunt damping adaptive to environmental conditions. Hagood and von Flotow [44] showed that a series resistor-inductor (RL) circuit connected across the electrodes of a piezoelectric bimorph can be utilized to dissipate base vibrations, similar to conventional mechanical damping. Wu and Joseph have displayed the use of a single Lead Zirconate Titanate (PZT) for multi-modal shunt damping [45, 46] while Fleming et al. [47], has further

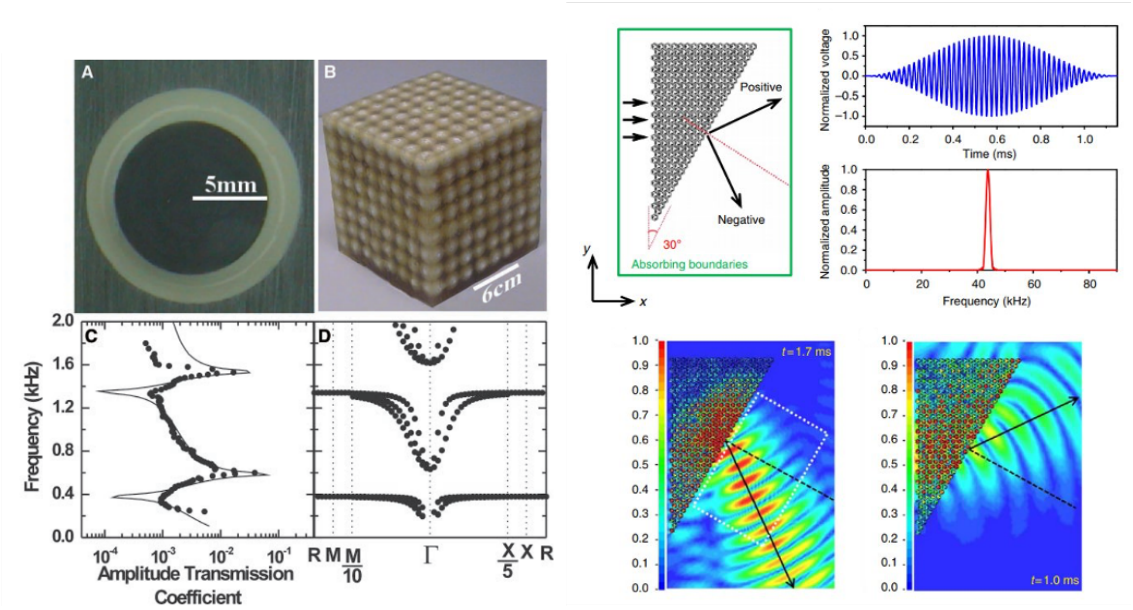

(a) (b)

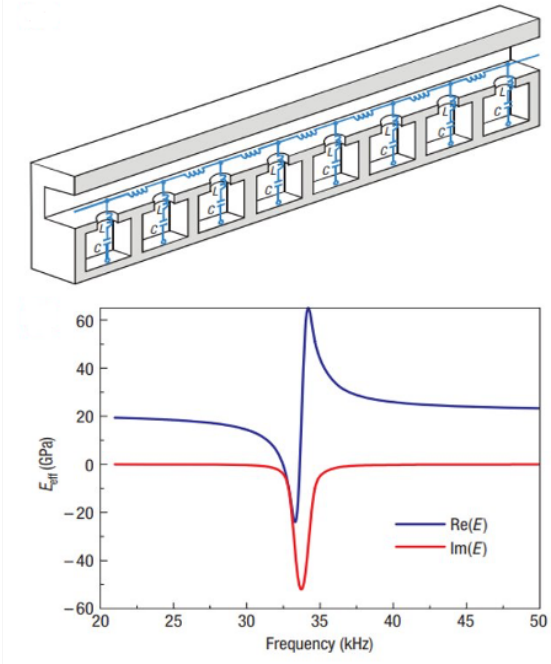

(c)

Figure 1.3: (a) Liu et al. shows negative density application of metastructures [33]. (b) Structure demonstrating negative refractive index [35]. (c) Negative modulus as displayed by Fang et al. [36].

researched upon optimization of multi-mode implemented PZT damping using synthetic impedance circuits and controlled voltage source. Similarly, non-linear shunt damping [48,

49] has also been introduced for vibration isolation.

1.5 Nonlinear Vibration Attenuation and Energy Harvesting

Locally resonant metastructures make use of mechanical resonators in order to attenuate vibrations at their respective resonant frequencies. Most research efforts, however, target linear configurations of beams to attain the desired bandgap. This omits a whole other world of nonlinearity where much extensive motion dynamics of the beam are involved reaching subharmonic, superharmonic and chaotic resonance behaviors. These nonlinear oscillators provide an advantage over their linear counterparts in allowing much wider frequency bandwidth. Furthermore, the intrawell, interwell and chaotic vibrations of nonlinear oscillator configurations extend upon the enhanced wideband behavior based on the provided input amplitudes [8, 50–53]. Nonlinear energy sinks have been researched upon to obtain vibration attenuation. However, most of these works are either focused on utilizing simpler linear oscillators or low degree of freedom systems in conjunction with bistable attachments [54–58]. Focusing on metastructure based nonlinear configurations, research extends towards Duffing-type cubic hardening nonlinear resonators by Lazarov et al. [59], or the numerical investigation of cubic hardening effects on spring-mass system by Banrjee et al. [60, 61]. Casalotti et al. [62] also focused on demonstrating amplified vibration attenuation in a nonlinear metamaterial beam. Xia et al. [63, 64] utilized both lumped and distributed parameter models to demonstrate the enhancement of nonlinear bandgap under various acceleration levels for a metamaterial beam with bistable attachments. However, not much work has been done in a metamaterial type setting related to nonlinear oscillators. Adding to the nonlinear attenuating characteristics of such bistable attachments, research is still undergoing to attain simultaneous benefits as with linear metatructures. Sandra et al. [65] displayed the vibrational energy harvesting characteristics from impulsive excitations of bistable attachments; Patrick et al. [66] showed the effect of VEH behavior using nonlinearity in auxiliary bistable harvesting modules; Romeo et al. [67] studied the low-energy

transfer behavior in nonlinear bistable systems. Similarly, Harne et al. [68] has studied the superharmonic dynamics of bistable energy harvesters using linear oscillators. The potential of nonlinear bistable attachments under the light of aforementioned studies can greatly be realized using transient dynamics for vibration attenuation in conjunction with harnessing useful power. Hence, such characteristics of nonlinear resonators can be used to develop oscillators targeting the desired frequency range for both vibration attenuation and simultaneous power generation.

1.6 Thesis Outline

This thesis explores piezoelectric energy harvesting in multifunctional electromechanical metastructures. Chapter 2 numerically and experimentally investigates piezoelectric energy harvesting on a locally resonant mechanical linear metamaterial beam for concurrent power generation and bandgap formation. The first part of the chapter reviews the governing equations [69] for the locally resonant energy harvesting metastructure along with the corresponding numerical results and experimental setup. The latter part expands the experimental results incorporating parameter identification for a single resonator and extending it to the complete metastructure with 9 pairs of cantilever-type piezoelectric energy harvesters. Chapter 3 focuses on the same characteristics in electromechanical metastructures. In comparison to mechanical structures, this chapter focuses on using electromechanical resonators which help in creating a bandgap at the desired frequency without making additional changes such as varying the resonator mass. Furthermore, it shows how resistance loading affects this bandgap and correspondingly, how useful power can be harnessed alongside the desired vibration reduction. The initial part of the chapter starts with reviewing a framework of governing equations using a distributed parameter model and application of modal analysis to understand the performance of such finite-sized structures. Then it extends on the theoretical work of Sugino et al. [69] and establishes numerical and experimental results for simultaneous bandgap formation and VEH capabilities of the locally

resonant electromechanical metastructure. Chapter 4 transitions from linear to nonlinear (bistable) attachments and elaborates on its attenuation and harvesting capabilities. It details on utilizing the chaotic nonlinear behavior of bistable attachments under various base excitation amplitudes for a wider bandwidth. Subsequently, it builds up on the recent work of Xia et al. [63] and starts with a modal analysis approach. Then it proceeds towards describing the experimental setup and results of up and down frequency sweeps. Finally, chapter 5 concludes the dissertation by summarizing the results of the research detailed in this thesis.

CHAPTER 2

LINEAR MECHANICAL LOCALLY RESONANT PIEZOELECTRIC ENERGY HARVESTING METASTRUCTURE

Completely mechanical metastructures are categorized as those which utilize mechanical resonators as vibration absorbers. These tend to add mass to the structure which define the respective bandgap for the mechanical case. These help in both low-frequency vibration mitigation and low-power VEH capabilities. This chapter deals with such a mechanical metastructure beam.

2.1 Locally Resonant Energy Harvesting Metastructure

2.1.1 Mechanical Model

We consider a locally resonant metastructure with attached piezoelectric energy harvesters, shown schematically in Figure 2.1. Following the analysis of Sugino and Erturk [26], we have the following governing equation for the forced vibrations of a distributed parameter system:

$$\mathcal{L}[w(\mathbf{P},t)] + \left[m(\mathbf{P}) + \sum_{j=1}^{S} m_{p,j}\delta(\mathbf{P}-\mathbf{P}_j)\right]\ddot{w}(\mathbf{P},t) - \sum_{j=1}^{S}(k_j u_j(t) + c_j \dot{u}_j(t))\delta(\mathbf{P}-\mathbf{P}_j) = f(\mathbf{P},t) \tag{2.1}$$

Here $\mathcal{L}$ is the stiffness operator of order $2p$ where $p \geq 1$ defining the order of the system [70, 71], $w(\mathbf{P},t)$ is the displacement of point $\mathbf{P}$ at time t where $\mathbf{P}\in D$, $m(\mathbf{P})$ is the mass distribution at $\mathbf{P}$, S is the number of resonators, $\delta(\mathbf{P})$ is the Dirac delta function and $f(\mathbf{P},t)$

is the external forcing. The corresponding resonator equations are as follows:

$$m_j\ddot{u}_j + c_j\dot{u}_j + k_j u_j - \theta_j v_j = -m_j\ddot{w}(\mathbf{P}_j, t) \tag{2.2}$$

$$C_{p,j}\dot{v}_j + \mathscr{Y}_j[v_j] + \theta_j\dot{u}_j = 0 \tag{2.3}$$

where k_j, c_j, m_j, $m_{p,j}$, u_j and $\mathbf{P}_j$ are the stiffness, mechanical damping coefficient, mass, mass of clamping hardware, displacement and position of the jth resonator respectively. θ_j, $C_{p,j}$ and $\mathscr{Y}_j$ are the electromechanical coupling, piezoelectric capacitance and admittance of the shunt circuit on the jth resonator.

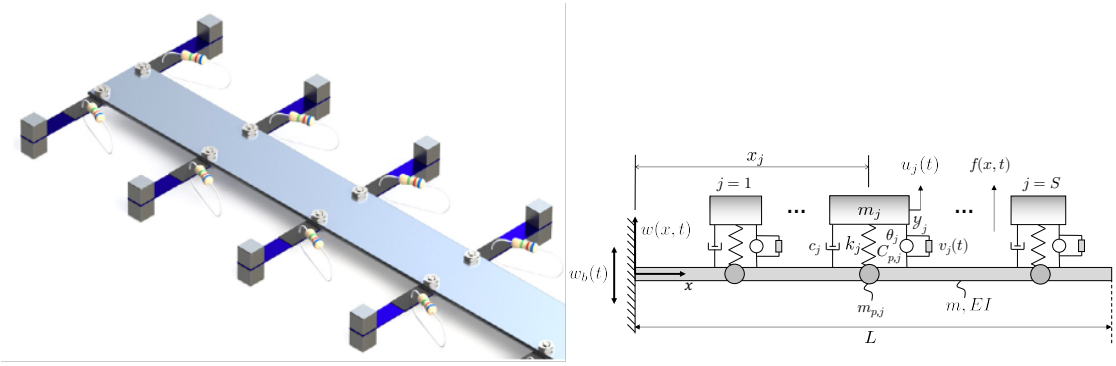

(a) (b)

Figure 2.1: (a) Locally resonant energy harvesting metastructure with cantilever beams containing mechanical resonators and piezoelectric patches. (b) Schematic representation of the energy harvesting metastructure.

Using a modal expansion procedure for the structure mode shapes without the resonators, we have the following approximate solution:

$$w(\mathbf{P}, t) = \sum_{r=1}^{N} \eta_r(t)\phi_r(P) \tag{2.4}$$

where N is the number of modes, ϕ_r is the rth mode shape and η_r is the corresponding

modal weighing. These mode shapes satisfy the orthogonality conditions given by:

$$\int_D m(\mathbf{P})\phi_r(\mathbf{P})\phi_s(\mathbf{P})dD = \delta_{rs} \tag{2.5}$$

$$\int_D \phi_r(\mathbf{P})\mathcal{L}[\phi_s(\mathbf{P})]dD = \omega_r^2\delta_{rs} \tag{2.6}$$

Here, ω_r is the natural frequency of the plain structure at the rth mode shape. Substituting Equation 2.4 into Equation 2.1, multiplying by mode shape ϕ_k, integrating across the domain D and applying orthogonality conditions, we obtain the discretized governing equation:

$$\left(\delta_{rk} + \sum_{j=1}^{S} m_{p,j} \sum_{k=1}^{N} \phi_r(\mathbf{P}_j)\phi_k(\mathbf{P}_j)\right)\ddot{\eta}_k + 2\zeta_r\omega_r\dot{\eta}_r + \omega_r^2\eta_r - \sum_{j=1}^{S}(k_j u_j + c_j\dot{u}_j)\phi_r(\mathbf{P}_j) = q_r, \tag{2.7}$$

where ζ_r is the modal damping factor for the rth mode shape and:

$$q_r(t) = \int_D \phi_r(\mathbf{P})f(\mathbf{P},t)dD \tag{2.8}$$

Now, substituting Equation 2.4 into Equation 2.2 and Equation 2.3 gives the discretized equations for the resonators:

$$m_j\ddot{u}_j + c_j\dot{u}_j + k_j u_j - \theta_j v_j = -m_j\sum_{r=1}^{N}\phi_r(P_j)\ddot{\eta}_r \tag{2.9}$$

$$C_{p,j}\dot{v}_j + \mathscr{Y}_j[v_j] + \theta_j\dot{u}_j = 0 \tag{2.10}$$

Taking the Laplace transform of Equation 2.7, Equation 2.9, and Equation 2.10, and rear-

ranging, we have the following linear equation:

$$\left(\delta_{rk} + \sum_{j=1}^{S} m_{p,j} \sum_{k=1}^{N} \phi_r(\mathbf{P}_j)\phi_k(\mathbf{P}_j)\right) s^2 H(k) + (2\zeta_r\omega_r s + {\omega_r}^2)H_r(s) + \frac{s^2(2\zeta\omega_t s + {\omega_t}^2)\sum_{j=1}^{S} m_j\phi_r(\mathbf{P}_j)\sum_{k=1}^{N}\phi_k(\mathbf{P}_j)H_k(s)}{s^2 + 2\zeta\omega_t s + {\omega_t}^2\left(1 + \frac{\gamma s}{s+h(s)}\right)} = Q_r(s) \tag{2.11}$$

where $H_r(s)$ and $Q_r(s)$ are the Laplace transforms of $\eta_r(t)$ and $q_r(t)$ respectively. For each resonator, $\omega_t^2 = \frac{k_j}{m_j}$ is the short-circuit resonant frequency and $\zeta = \frac{c_j}{2\omega_t m_j}$ is the damping ratio. Furthermore, $h(s) = \frac{Y_j(s)}{C_{p,j}}$ is the admittance of the shunt harvesting circuit ($Y_j(s)$ is the Laplace transform of $\mathscr{Y}_j$), and $\gamma = \frac{\theta_j^2}{k_j C_{p,j}}$ is the dimensionless coupling term with the assumption that it is identical for each resonator.

Introducing the dimensionless parameter μ defined as the ratio of total resonator masses to the mass of the plain structure, the resonator masses m_j can be obtained by setting them proportional to the distributed mass at the specified resonator locations $m(\mathbf{P})$. Thus:

$$m_j = \mu m(\mathbf{P}_j)\Delta D_j \tag{2.12}$$

where ΔD_j is a portion of the domain D around the jth resonator. With these simplifications, we obtain the following equation for a finite number of resonators:

$$(s^2 + 2\zeta_r\omega_r s + {\omega_r}^2)H_r(s) + s^2\left[m_j\frac{(2\zeta\omega_t s + \omega_t^2)}{s^2 + 2\zeta\omega_t s + \omega_t^2\left(1 + \frac{\gamma s}{s+h(s)}\right)} + m_{p,j}\right] \times \sum_{k=1}^{N} H_k(s)\sum_{j=1}^{S}\phi_r(\mathbf{P}_j)\phi_k(\mathbf{P}_j) = Q_r(s) \tag{2.13}$$

Equation 2.13 is then utilized in the next section to obtain numerical results for the locally resonant bandgap and useful power output corresponding to the model in Figure 2.1.

2.2 Numerical Results

For the numerical simulations, we consider an aluminum beam with 20 harvesters (S) at a target frequency ratio $\frac{\omega_t}{\omega_1} = 75$. It is clamped at one end ($x = 0$) and vibrates freely at the other end ($x = L$). It has a width of w, a thickness of h and a length L. The beam has a mass density of ρ and a Young's modulus of E. It has a mass per length of m_b with S resonators attached to it.

We consider purely resistive shunt circuits to quantify the power output of the energy harvesters, corresponding to normalized shunt admittance $h(i\omega) = \frac{1}{\tau}$, where $\tau = RC_{p,j}$ is the circuit time constant and R is the load resistance. At each frequency of excitation, the optimal load τ_{opt} that gives the maximum power output from the full metastructure is obtained. Figure 2.2 shows the total optimal real power output of the mechanical metastucture versus normalized load and frequency with finite (20) harvesters. It is clear from the figure that the maximum broadband power output occurs near the resonant frequency which in this case is $\frac{\omega_t}{\omega_1} = 75$, immediately before the resonant bandgap. The dashed line here shows optimal loading at each excitation frequency.

For the same model, the power outputs for individual harvesters at the optimal load for the full metastructure were plotted to identify the harvesters which output the maximum power. As expected, Figure 2.3 shows how the harvesters near the excited base yield the maximum power. Only the first 9 harvesters have been shown here since a trend can be observed that at the specified target frequency, power output from the harvesters decreases as we move from the first harvester to the twentieth, which makes it redundant to show the remaining 11 harvesters as well.

The effect of optimal power as we move along the beam from the first harvester towards the last one, 20^{th} in this case, can be seen in Figure 2.4a. After the first 10 harvesters, the trend in power output is more or less arbitrary since it becomes very minimal and hence negligible. This is plotted for constant normalized target frequency ratios of 25, 50, 75 and

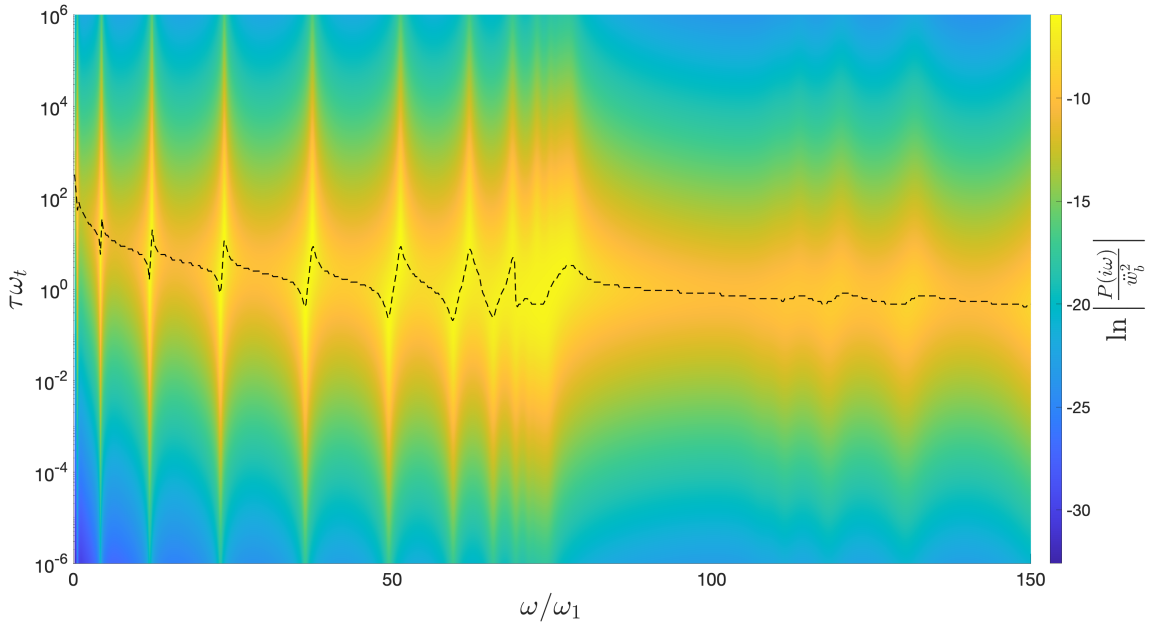

Figure 2.2: Optimal total power of the mechanical metastucture versus time constant and normalized frequency.

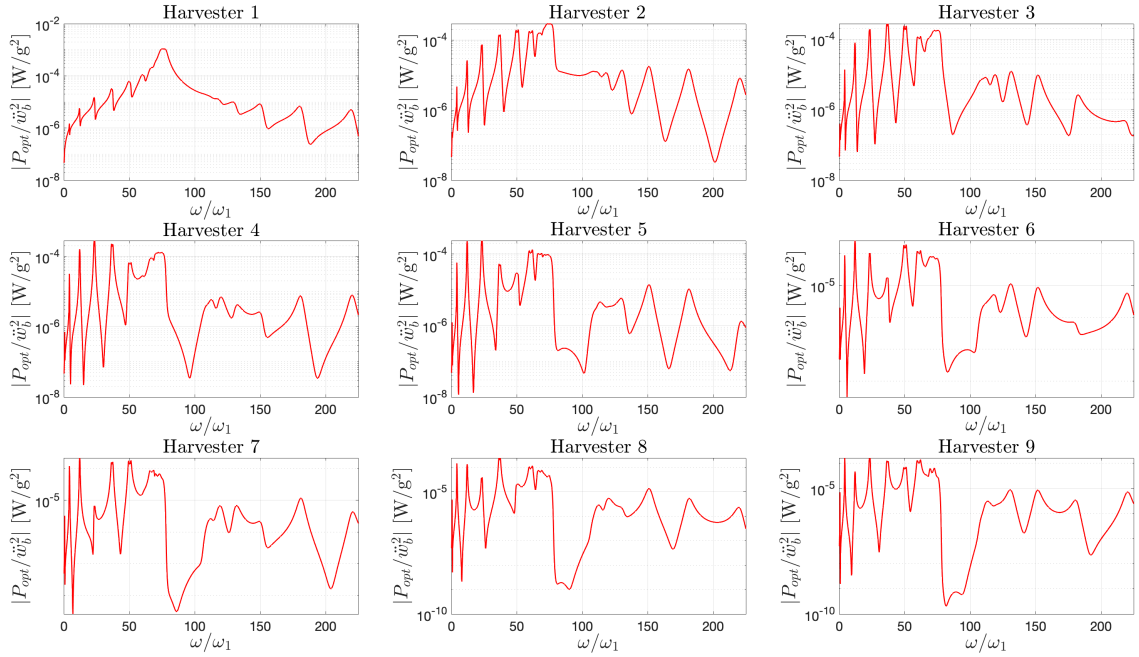

Figure 2.3: Optimal power output for the first nine harvesters at $\frac{\omega_t}{\omega_1} = 75$.

100; all of which have the same trend in power output. Targeting lower vibration mode neighborhood (more flexible modes) results in higher power output, however, the trend with harvester index is similar.

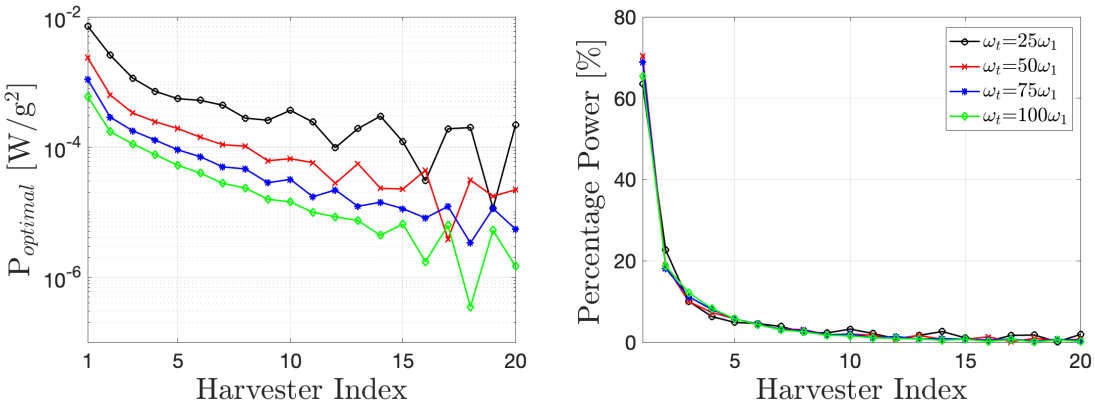

(a) (b)

Figure 2.4: (a) Optimal power versus harvester index. (b) Percentage power contribution as a function of harvester index.

The percentage power contribution as a function of harvester index for the same 20 harvesters along the beam is plotted in Figure 2.4b. As can be observed in this figure, the typical power distribution profile of the harvesters does not change significantly even when a higher vibration mode neighborhood is targeted. The first two harvesters are responsible for 65% and 22% of the total power contribution for each case of normalized frequency and it decreases towards the last one. As previously mentioned, and can be seen in Figure 2.4b, power contribution by harvesters after the first 10 is nearly negligible and can be omitted. Finally, Figure 2.5 shows the tip transmissibility at the target frequency. This is at the optimal value of τ_{opt} where vibrations can be seen to be attenuated in the bandgap.

Keeping the above-mentioned discussion in check, only 9 harvesters were used experimentally in the next section as a more practical measure since not only these have a significant contribution towards the total power output by the complete metastructure but using more than 9 harvesters crowds the main beam and hinders efficiency of the experiments.

2.3 Experimental Results

The practical system under consideration comprises a main beam with 9 cantilever attachments. Each small cantilever beam comprises two identical mechanical resonators with

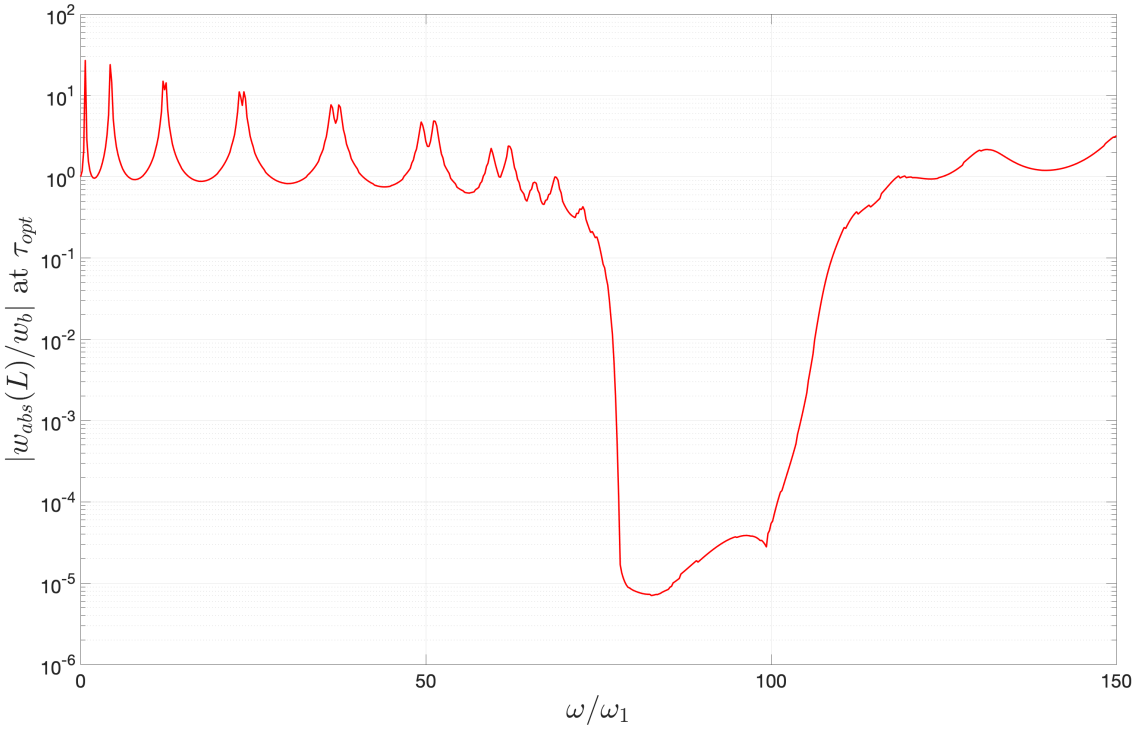

Figure 2.5: Tip transmissibility at τ_{opt} for $\frac{\omega_t}{\omega_1} = 75$ with 20 harvesters.

tip masses. Piezoelectric patches are placed at the base of each cantilever on both sides of the main beam connected to electrical loads (resistances) in order to quantify the electrical output from these sensors in the locally resonant bandgap neighborhood. The main beam is excited using an electrodynamic shaker within the frequency range of 0-150 Hz and the corresponding tip displacement is measured via a laser Doppler vibrometer (LDV) which extracts the transmissibility frequency response. Voltage output from each piezoelectric element is also recorded for each value of the electrical load. A resistance sweep is performed after bandgap confirmation to obtain the optimal electrical load for maximum power output. The experimental setup is shown in Figure 2.6.

2.3.1 Energy Harvester - Resonator Characterization

The single isolated resonator shown in Figure 2.7 is modeled as described in this section.

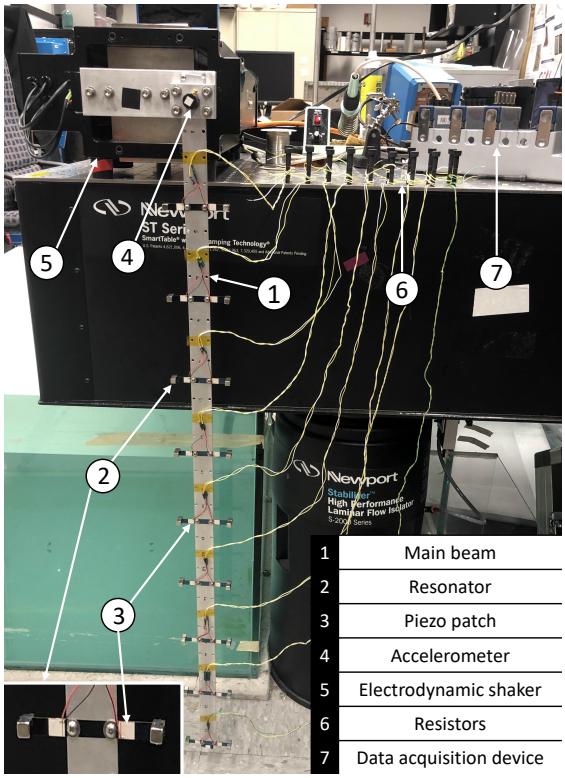

Figure 2.6: Experimental setup consisting of the main beam with nine resonators attached to electrical loads.

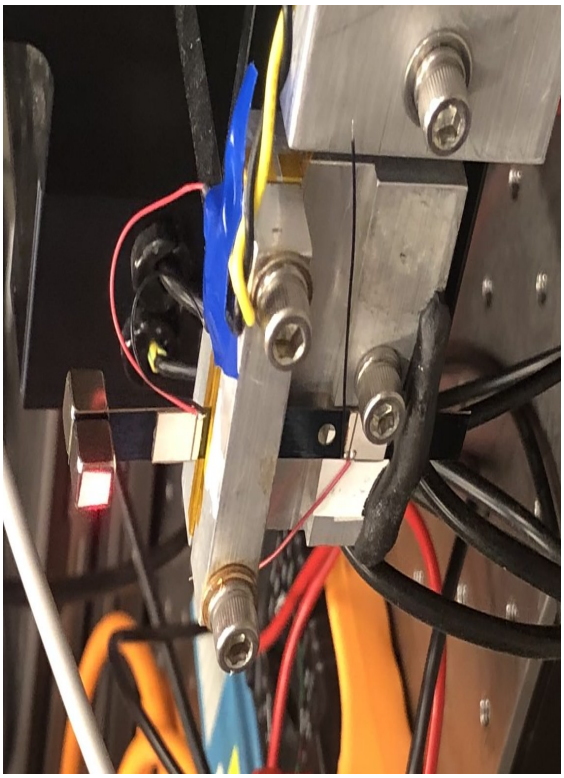

Figure 2.7: Single isolated resonator setup clamped to the shaker.

Governing Equations:

A lumped parameter model is used for the isolated single resonator since the mass of the cantilever beam is negligible compared to the resonator (tip) mass. This allows for the assumption to be relatively accurate. Figure 2.8 shows the corresponding schematic for the model.

The resonator governing equations with piezoelectric coupling for the single resonator model are as follows:

$$m\ddot{z} + c\dot{z} + kz - \theta v = -m\ddot{y} \tag{2.14}$$

$$C_p\dot{v} + \frac{1}{R_l}v + \theta\dot{z} = 0 \tag{2.15}$$

where m is the concentrated tip mass, k is the stiffness of the cantilever beam modeled as

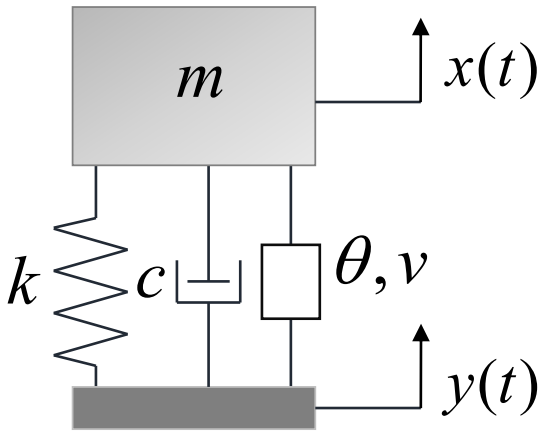

Figure 2.8: Lumped parameter model for single resonator.

a spring, c is the mechanical damping coefficient, θ is the electromechanical coupling, v is the voltage output obtained across the load, x is the mass displacement, y is the base displacement, z is the relative displacement between the mass and the base, C_p is the effective piezoelectric capacitance and R_l is the load resistance.

For harmonic base excitation, by letting $x = Xe^{i\omega t}$, $y = Ye^{i\omega t}$, $z = Ze^{i\omega t}$ and $v = Ve^{i\omega t}$, we obtain the following FRF:

$$\frac{X}{Y} = \frac{m\omega^2}{(k - m\omega^2 + i\omega c) + \frac{i\omega\theta^2}{i\omega C_p + \frac{1}{R_l}}} + 1 \tag{2.16}$$

$$\frac{V}{Y} = \frac{-im\omega^3\theta}{(k - m\omega^2 + i\omega c)\left(i\omega C_p + \frac{1}{R_l}\right) + i\omega\theta^2} \tag{2.17}$$

where X is the absolute response amplitude, Y is the base response amplitude and Z is the relative response amplitude. Equation 2.16 expresses the transmissibility FRF of the model (per base displacement) whereas Equation 2.17 defines the voltage FRF of the model (per base displacement). For plotting, the voltage and power FRFs were normalized with respect to base acceleration for a more conventional representation.

Parameter Identification:

To estimate parameters for the locally resonant metastructure, a single energy harvester was isolated from the full structure as shown in Figure 2.7. Experiments were performed by mounting the cantilever to an electrodynamic shaker for base excitation. An accelerometer was mounted to the shaker to measure input acceleration while the tip velocity of the cantilever was measured using an LDV. The voltage output from the piezoelectric patch (across each load resistance) was also measured during experiments.

Parameters for the lumped-element model (Equation 2.2 and Equation 2.3) were obtained from the experimental FRFs. The lumped mass m was approximated as the mass of the magnets placed on the tip of the cantilever, since the tip mass was much greater than the cantilever mass. The mechanical damping coefficient was measured using the experimental FRFs via the quality factor (Q) given as:

$$Q = \frac{f_r}{\Delta f} \tag{2.18}$$

where f_r is the resonant frequency and Δf is the half-power bandwidth corresponding to short circuit (SC) or open circuit (OC) half-power points $\left(f_{SC,OC} = \frac{|TR|_{SC,OC}}{\sqrt{2}}\right)$. The corresponding damping ratio ζ and the damping coefficient were then calculated as

$$\zeta = \frac{1}{2Q} \tag{2.19}$$

$$c = 2\zeta\sqrt{mk} \tag{2.20}$$

The equivalent stiffness k was estimated using the experimental SC resonant frequency f_{SC} as

$$k = (2\pi f_{SC})^2 m \tag{2.21}$$

Using the OC resonant frequency f_{OC}, the electromechanical coupling θ was calculated as

$$\theta = \sqrt{C_p(m(2\pi f_{OC})^2 - k)} \tag{2.22}$$

where C_p is the measured capacitance of the piezoelectric unit cell attached to the spring steel cantilever. The experimental results are shown in Figure 2.9, and the experimentally identified parameters are shown in Table 2.1.

Experimental data was obtained for the single resonator using NI Signal Express. The transmissibility and voltage FRFs obtained from the experiment (and then the power FRFs were calculated) which were then plotted against the model FRFs for each load resistance to verify that the model matches accurately with the experimentally obtained results. At all the load resistances mentioned in Table 2.1, this can be seen in Figure 2.9. Using experimental data obtained for the given single resonator, parameters were identified in order to obtain model FRFs by substituting these in Equation 2.2 and Equation 2.3. A summary of these parameter values can be seen in Table 2.1. Figure 2.9a reveals that with increasing load resistance, frequency shift and vibration attenuation occur. This shift in frequency appears as a transition of the system from SC ($R_l \rightarrow 0$) to OC ($R_l \rightarrow \infty$) conditions. From Figure 2.9b, we can see that at exactly SC, there is no voltage output and hence no voltage FRF can be obtained. However, it can be observed that as load resistance moves towards higher resistance values (or towards exact OC), it converges to a maximum value [72]. Figure 2.9c shows that the power output at each load resistance varies for a particular frequency ranging between the fundamental SC and OC resonant frequencies. This variation is, however, not the same for all resistances and here, the optimal loading and respective maximum power is obtained for a load resistance of $887\,\mathrm{k}\Omega$ ($f = 77.8\,\mathrm{Hz}$). It can be observed here that the modeled voltage and power FRFs present a good match with the experimental data and therefore, parameters estimated here are acceptable and good to use in the complete metastructure.

Using the experimental data obtained for the given single resonator, parameters were

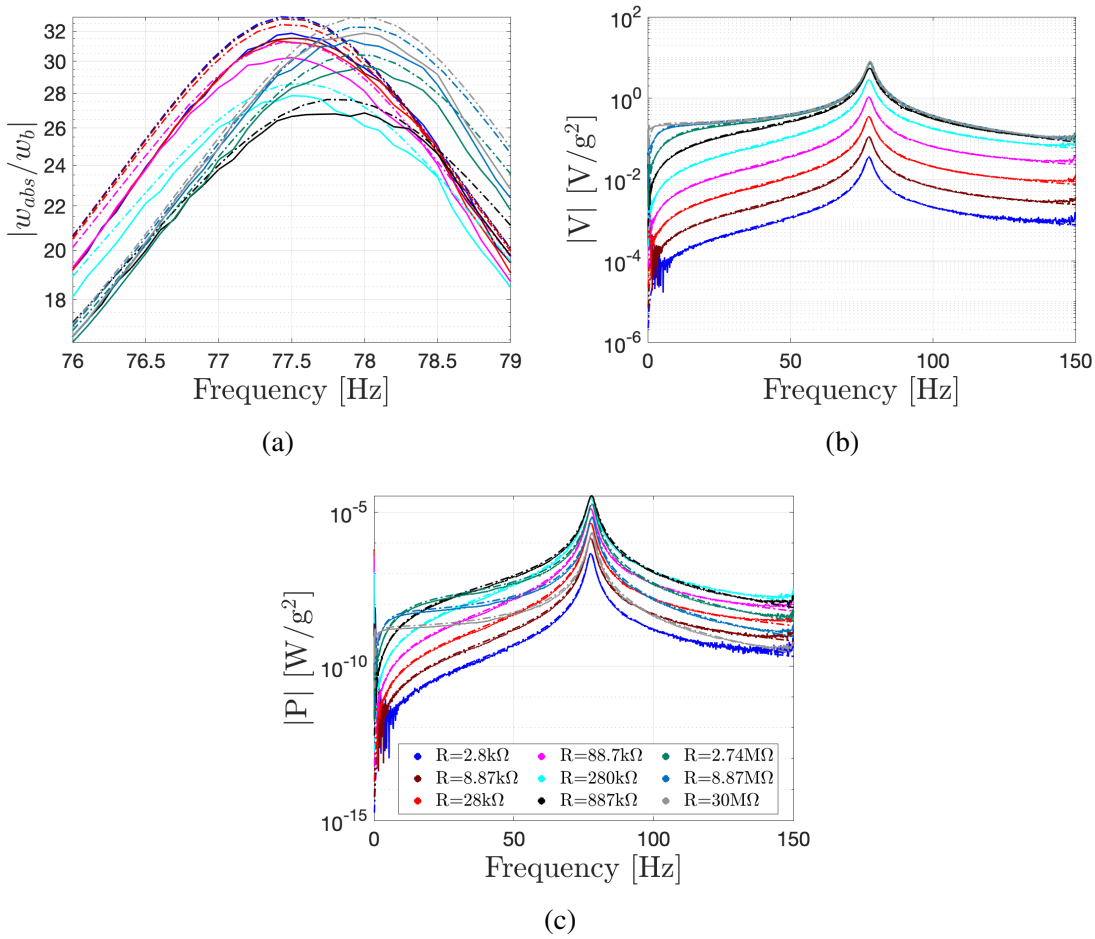

Figure 2.9: (a) Transmissibility comparison at all resistances for the single harvester. (b) Voltage output comparison at all resistances for the single harvester. (c) Power output comparison at all resistances for the single harvester. Dashed line in the figures corresponds to the model whereas solid line represents experimental data.

identified in order to obtain model FRFs by substituting these in Equation 2.2 and Equation 2.3. A summary of these parameter values can be seen in Table 2.1. It is to be noted that the lowest resistance of $2.8\,\mathrm{k}\Omega$ used here is very close to the SC conditions ($R_l \to 0$) whereas the highest resistance of $30\,\mathrm{M}\Omega$ resembles the OC conditions ($R_l \to \infty$).

Figure 2.9a reveals that with increasing load resistance, frequency shift and vibration attenuation occur. The shift in frequency appears as a transition of the system from SC to OC conditions. The zoomed-in figure also shows the attenuated vibrations with the increase in load resistance (e.g., 31.85 at $2.8\,\mathrm{k}\Omega$ to 30.23 at $28\,\mathrm{k}\Omega$).

Table 2.1: Estimated parameters for the single resonator.

m – resonator tip mass	$0.0036\,\mathrm{kg}$
c – mechanical damping coefficient	$0.0525\,\mathrm{N/m/s}$
k – spring steel stiffness	$853.63\,\mathrm{N/m}$
θ – electromechanical coupling	-$1.8884 \times 10^{-4}\,\mathrm{N/V}$
C_p – capacitance	$3.23 \times 10^{-9}\,\mathrm{F}$
R_l – load resistances	$2.8\,\mathrm{k\Omega}$, $8.87\,\mathrm{k\Omega}$, $28\,\mathrm{k\Omega}$, $88.7\,\mathrm{k\Omega}$, $280\,\mathrm{k\Omega}$, $887\,\mathrm{k\Omega}$, $2.74\,\mathrm{M\Omega}$, $8.87\,\mathrm{M\Omega}$, $30\,\mathrm{M\Omega}$

From Figure 2.9b, we can see that as the load resistance increases, so does the corresponding voltage output, harvested from the piezoelectric sensor. At exactly SC, there is no voltage output and hence no voltage FRF can be obtained. However, it can be observed that as load resistance moves towards higher resistance values (or towards exact OC), it converges to a maximum value [72]. Figure 2.9c shows that the power output at each load resistance varies for a particular frequency ranging between the fundamental SC and OC frequencies since power is proportional to the square of voltage output from the piezoelectric energy harvester. This variation is, however, not the same for all resistances and here. Specifically, the optimal loading and respective maximum power is obtained for a load resistance of $887\,\mathrm{k\Omega}$ ($f = 77.8\,\mathrm{Hz}$).

It can be observed here that the modeled voltage and power FRFs present a good match with the experimental data and therefore, parameters estimated here are acceptable and good to use with the complete metastructure.

2.3.2 Energy Harvesting Metastructure

Following the single resonator parameter identification case, experimental results were obtained for the complete metastructure for all load resistances as shown in Figure 2.6. Transmissibility and power FRFs were plotted for each resistance value and optimal loading was identified. It was then compared with the modeled system as described in previous sec-

tion using the individual harvester parameters in Table 2.1 and the main (primary) beam parameters summarized in Table 2.2 . For the sake of brevity, model and experimental data comparison has only been shown for a load resistance of $88.7\,\mathrm{k}\Omega$, which yielded the maximum power output among all load resistances that were tested. The experimental and model tip transmissibility, power output, and percentage power contribution are shown in Figure 2.10.

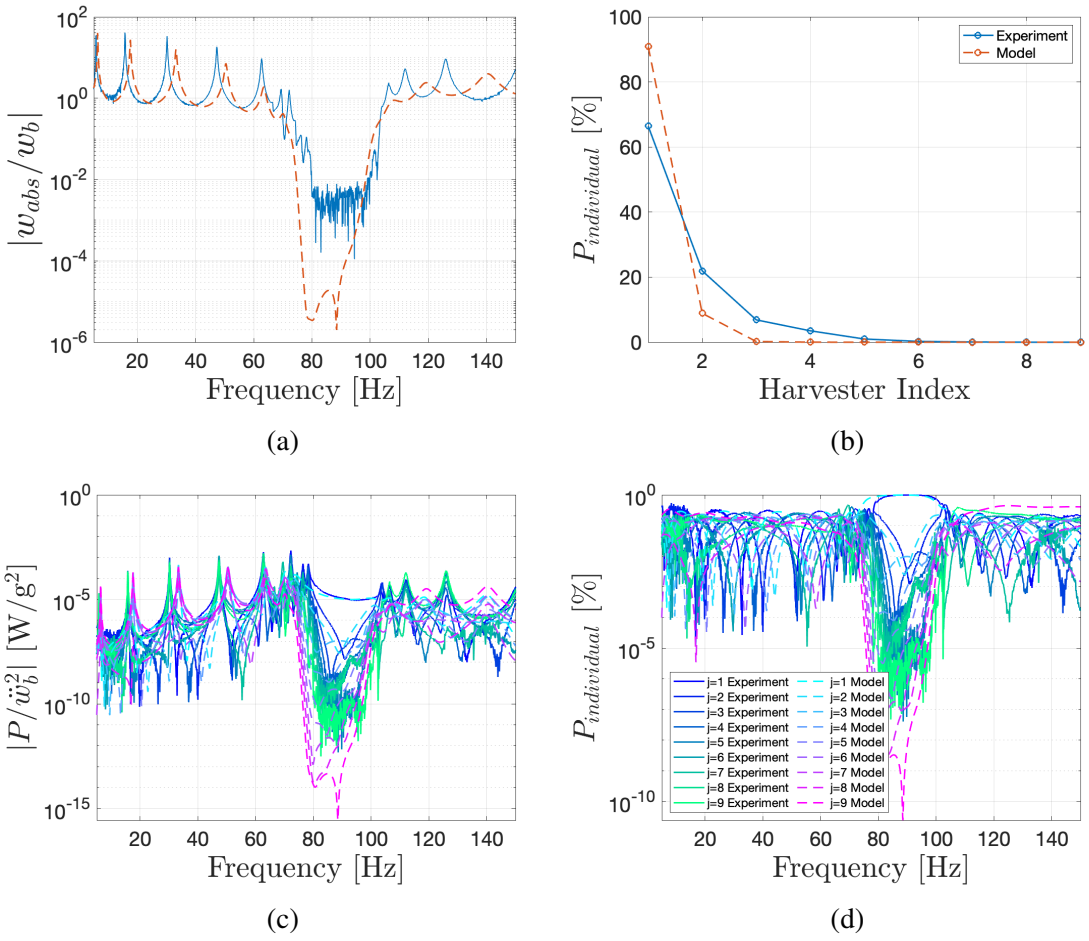

Figure 2.10: (a) Transmissibility comparison versus frequency. (b) Percentange power contribution comparison as a function of harvester index. (c) Power output comparison of each harvester. (d) Percentage power contribution comparison versus frequency. All comparison between experimental and model data has been done at $R_l = 88.7\,\mathrm{k}\Omega$.

Figure 2.10 shows that the model matches well with the experimental data. The tip transmissibility in Figure 2.10a shows that a locally resonant bandgap was created in the

system. The discrepancy seen in the graphs is as expected since the model does not take into account physical constraints and various imperfections that would break periodicity, especially when the beam tip displacement and power output are highly sensitive to the excitation frequencies. It can also be added that the focus of this research was towards the bandgap than matching individual modes where they were assumed to have the same damping ratio. The model, therefore, is experimentally verified and thus the use of energy harvesting circuitry with resonators can lead to useful power generation capabilities alongside its vibration attenuation properties for the locally resonant metastructure. Multiple comparisons of experimental and model systems have also shown that even though maximum power can be extracted at optimal loads, the bandgap largely remains insensitive to this loading and henceforth the structure can still be utilized for its attenuating characteristics. This is an important conclusion since it allows for development of metastructures with integrated energy harvesting capabilities which corresponds to an increase in their multifunctionality. This could be used in small sensors and devices requiring little power in such multifunctional applications where vibration suppression and energy harvesting are of combined interest.

For the individual power contribution by each harvester, it can be seen in Figure 2.10c that the harvester closest to the base contributes the most. Hence the harvester nearest to the area of excitation outperforms others in terms of useful power generation. Therefore, the analysis confirms that inside the locally resonant bandgap, most of the vibrational energy is concentrated near the base of the beam (and the corresponding useful energy harvested) and gradually decreases as we move towards the tip. Furthermore, this power output is concentrated and maximum right at the start of the bandgap.

To verify these experimental results, a modeled system was plotted against the experimental data. Some important assumptions in this case were as follows:

- It was assumed that all resonators along with the corresponding spring steel were identical in nature having the same parameters

- A modal damping $\zeta_r = 0.01$ was used for all vibrational modes and assumed to be the same for each one
- A target frequency ratio of $77.8\,\mathrm{Hz}$ was used towards the complete beam obtained from the single resonator experiment

A complete parameter list for the complete beam model can be seen in Table 2.2.

Table 2.2: Parameters used for the modeled system.

m – resonator tip mass	$0.0036\,\mathrm{kg}$
c – mechanical damping coefficient	$0.0525\,\mathrm{N/m/s}$
k – spring steel stiffness	$853.63\,\mathrm{N/m}$
θ – electromechanical coupling	-$1.8884 \times 10^{-4}\,\mathrm{N/V}$
C_p – capacitance	$3.23 \times 10^{-9}\,\mathrm{F}$
R_l – load resistances	$2.8\,\mathrm{k\Omega}$, $8.87\,\mathrm{k\Omega}$, $28\,\mathrm{k\Omega}$, $88.7\,\mathrm{k\Omega}$, $280\,\mathrm{k\Omega}$, $887\,\mathrm{k\Omega}$, $2.74\,\mathrm{M\Omega}$, $8.87\,\mathrm{M\Omega}$, $30\,\mathrm{M\Omega}$
E – Young's modulus	$70 \times 10^9\,\mathrm{Pa}$
w – width of the beam	$0.0254\,\mathrm{m}$
h – thickness of the beam	$1.49 \times 10^{-3}\,\mathrm{m}$
ρ – density	$2700\,\mathrm{kg/m^3}$
L – length of beam	$0.9144\,\mathrm{m}$
m_b – mass per length of beam	$0.0985\,\mathrm{kg/m}$
m_c – mass of clamps	$0.0017\,\mathrm{kg}$
ω_1 – fundamental frequency	$9.236\,\mathrm{rad/s}$

2.4 Conclusion

Vibrational energy exists around us which can be undesired but useful in some cases. There is interest in not only attenuating the corresponding vibration but also utilizing the energy for our own benefit. This is currently a growing field and warrants a great amount of in-depth understanding to achieve the described goals. So far multiple ways have been

developed to simultaneously work towards these. This chapter tries to bridge these benefits by using piezoelectric sensors on LR metastructures to harness low-power output. A modal analysis of the described system is presented which reviews the governing empirical relations for the said objectives. Numerical analysis is then performed on the system to obtain simulated transmissibility and power output responses over a range of frequencies at various load resistances. Optimal loading is then identified and power output at this loading is plotted as a function of harvester index to observe the trend. Furthermore, a single harvester is isolated in order to estimate the beam parameters which were then utilized to perform experimental verification of the complete beam. It can be said from the analysis that indeed most of the vibrational energy is localized near the base of the beam and maximum power output can be obtained immediately before the bandgap at the specified target frequency ratio after validation of the bandgap for the defined number of resonators. Moreover, as we move further away from the harvester nearest to the area of excitation, the corresponding power output decreases. The following chapter discusses an electromechanical metastructure to verify its attenuation and harvesting capabilities.

CHAPTER 3

LINEAR ELECTROMECHANICAL LOCALLY RESONANT PIEZOELECTRIC ENERGY HARVESTING METASTRUCTURE

In comparison to mechanical metastructure beams, electromechanical LR metastructures make use of shunt impedance as resonators in order to simultaneously attenuate vibrations and allow for harvesting useful power. This is more agile than its mechanical counterpart because of the added flexibility of tuning the bandgap to the desired frequency in addition to providing ease of access in design. This chapter is centered on the aforementioned electromechanical metastructure characteristics.

3.1 Electromechanical Energy Harvesting Metastructure

3.1.1 Electromechanical Model

Consider a piezoelectric bimorph beam as shown in Figure 3.1 with continuous and symmetric segmented electrodes between its left ($x = x_j^L$) and right ($x = x_j^R$) positions sandwiching a central substrate, which can be seen in the schematic. Following the analysis performed by Sugino et al. [26, 69], the governing electromechanical equations under transverse force per unit length ($f(x,t)$) for linear bending vibrations of the beam and current balance in shunt circuits are:

$$EI\frac{\partial^4 w}{\partial x^4} + m\frac{\partial^2 w}{\partial t^2} - \theta\sum_{j=1}^{S} v_j(t)\frac{\partial^2}{\partial x^2}[H(x - x_j^L) - H(x - x_j^R)] = f(x,t) \tag{3.1}$$

$$C_{p,j}\dot{v}_j(t) + \mathscr{Y}_j[v_j(t)] + \theta\int_{x_j^L}^{x_j^R}\frac{\partial^3 w}{\partial x^2 \partial t}dx = 0, \qquad j = 1...S \tag{3.2}$$

where $j = 1...S$ are the number of electrodes, $w(x,t)$ is the transverse displacement of the beam, $v_j(t)$ is the voltage across the jth pair of electrodes, m is the mass of the segmented electrode, θ is the electromechanical coupling, $\mathscr{Y}_j$ and $C_{p,j}$ are the admittance and piezoelectric capacitance of the jth shunt circuit respectively, and $H(x)$ is the Heaviside function. Assuming no damping in the beam at this point (modal damping can always be added later), effective properties of the bimorph are:

$$EI = \frac{2b}{3}\left(c_s\frac{h_s^3}{3} + \bar{c}_{11}^E\left[\left(h_p + \frac{h_s}{2}\right)^3 - \frac{h_s^3}{8}\right]\right) \tag{3.3}$$

$$m = b(\rho_s h_s + 2\rho_p h_p) \tag{3.4}$$

$$\theta = \bar{e}_{31}\frac{b_e}{2h_p}\left[\left(h_p + \frac{h_s}{2}\right)^2 - \frac{h_s^2}{4}\right] \tag{3.5}$$

$$C_{p,j} = \bar{\varepsilon}_{33}^S\frac{b_e\Delta x_j}{2h_p} \tag{3.6}$$

Here, b is the width of the beam, ρ_p, h_p and b_e are the mass density, thickness and width of the piezoelectric layer respectively; $\bar{c}_{11}^E$, $\bar{e}_{31}$ and $\bar{\varepsilon}_{33}^S$ are the reduced 1D effective properties defined as elastic modulus at constant electric field, stress constant and permittivity component at constant stress, respectively, derived from the 3D constitutive equations:

$$\bar{c}_{11}^E = \frac{1}{s_{11}^E}, \qquad \bar{e}_{31} = \frac{d_{31}}{s_{11}^E}, \qquad \bar{\varepsilon}_{33}^S = \bar{\varepsilon}_{33}^T - \frac{d_{31}^2}{s_{11}^E} \tag{3.7}$$

where s_{11}^E is the elastic compliance at constant electric field, d_{31} is the piezoelectric strain constant and $\bar{\varepsilon}_{33}^T$ is the permittivity component at constant strain.

Using a modal expansion procedure for w, the transverse displacement of the beam is

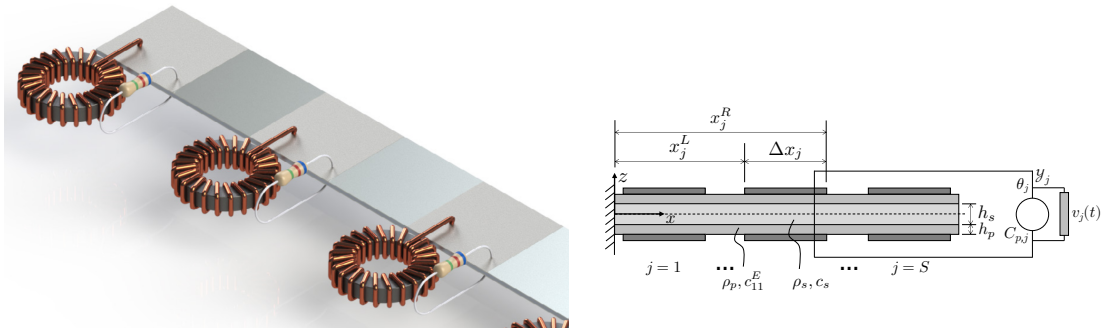

(a) (b)

Figure 3.1: (a) Electromechanical locally resonant energy harvesting metastructure containing piezoelectric bimorph with segmented electrodes. Inductors shunted to each pair of electrodes serve as electromechanical resonators, and resistors are placed in parallel to provide energy harvesting capability. (b) Schematic diagram of the metastructure under transverse force per unit length.

given by:

$$w(x,t) = \sum_{r=1}^{N} \eta_r(t)\phi_r(x) \tag{3.8}$$

where N is the number of modes, ϕ_r is the rth mode shape and η_r is the corresponding modal weighing. These mode shapes satisfy the orthogonality conditions given by:

$$\int_0^L m\phi_r(x)\phi_s(x)dx = \delta_{rs}, \qquad r,s = 1,2,... \tag{3.9}$$

$$\int_0^L EI\phi_r(x)\frac{d^4\phi_s}{dx^4}dx = {\omega_r}^2\delta_{rs}, \qquad r,s = 1,2,... \tag{3.10}$$

Here L is the length of the beam, ω_r is the natural frequency of the plain structure at the rth mode shape and δ_{rs} is the Kronecker delta. By substituting Equation 3.8 into Equation 3.1, multiplying by mode shape $\phi_k(x)$, integrating across the beam, we get the following governing equations in modal coordinates:

$$\ddot{\eta}_r(t) + \omega_r^2\eta_r(t) - \theta\sum_{j=1}^{S} v_j(t)\Delta\phi'_{r,j} = q_r(t) \tag{3.11}$$

$$C_{p,j}\dot{v}_j(t) + \mathscr{Y}_j[v_j(t)] + \theta \sum_{r=1}^{N} \Delta\phi'_{r,j}\dot{\eta}_r(t) = 0 \tag{3.12}$$

and $\Delta\phi'_{r,j}$ is the slope of the rth mode between the ends of the jth electrode and $q_r(t)$ is the modal forcing given as:

$$\Delta\phi'_{r,j} = \left(\frac{d\phi_r}{dx}\right)_{x_j^L}^{x_j^R} = \frac{d\phi_r}{dx}(x_j^R) - \frac{d\phi_r}{dx}(x_j^L), \qquad q_r(t) = \int_0^L \phi_r(x) f(x,t) dx \tag{3.13}$$

Taking Laplace transform of Equation 3.11 and Equation 3.12, we obtain the following two equations governing modal weighing and voltages:

$$(s^2 + \omega_r^2)H_r(s) + \frac{\alpha s}{s + h(s)} \sum_{j=1}^{S} EI \frac{\Delta\phi'_{r,j}}{\Delta x_j} \sum_{k=1}^{N} \frac{\Delta\phi'_{k,j}}{\Delta x_j} \Delta x_j H_k(s) = Q_r(s) \tag{3.14}$$

$$(sC_{p,j} + \mathscr{Y}_j(s))V_j(s) + s\theta^2 \sum_{r=1}^{N} \frac{\Delta\phi'_{r,j}}{s^2 + \omega_r^2} \sum_{k=1}^{S} \Delta\phi'_{r,k} V_k(s) = Q_j(s) \tag{3.15}$$

where α is a dimensionless parameter related to electromechanical coupling and $h(s)$ is the admittance of the shunt circuitry, assumed to be the same for each electrode pair, given as:

$$\alpha = \frac{2\theta^2 h_p}{EI\bar{\varepsilon}_{33}^S b_e} = \frac{\bar{e}_{31}^2 b_e h_p (h_s + h_p)^2}{2EI\bar{\varepsilon}_{33}^S}, \qquad h(s) = \frac{\mathscr{Y}_j(s)}{C_{p,j}} \tag{3.16}$$

Assuming a large number of unit cells such that an electrode pair becomes infinitesimal i.e. $S \to \infty$, we can use the following reasonable approximation for a finite number of electrodes:

$$\begin{aligned} &\lim_{S\to\infty} \lim_{\Delta x_j \to 0} \sum_{j=1}^{S} EI \frac{\Delta\phi'_{r,j}}{\Delta x_j} \sum_{k=1}^{N} \frac{\Delta\phi'_{k,j}}{\Delta x_j} \Delta x_j H_k(s) \\ &= \int_0^L EI \frac{d^2\phi_r}{dx^2} \sum_{k=1}^{N} \frac{d^2\phi_k}{dx^2} dx H_k(s) = \omega_r^2 H_r(s) \end{aligned} \tag{3.17}$$

Hence, incorporating modal damping ζ_r in Equation 3.14, response of the rth mode shape

can be written as:

$$H_r(s) = \frac{Q_r(s)}{s^2 + 2\zeta_r\omega_r s + \omega_r^2\left(1 + \frac{\alpha s}{s+h(s)}\right)} \tag{3.18}$$

For the purpose of this chapter, synthetic impedance shunt circuits are used to obtain numerical and experimental results utilizing the equations derived. This circuit acts as a voltage-controlled current source where the shunt circuit impedance can be tuned via digital filtering. A bandgap is expected around the target frequency $\omega_t/(2\pi)$ [73] and the corresponding power output is explored in this bandgap neighborhood.

3.2 Numerical Results

In order to numerically analyze the electromechanical model in Figure 3.1, we consider an aluminum beam with dimensions $16.8\,\mathrm{cm} \times 2.1\,\mathrm{cm} \times 0.5\,\mathrm{mm}$ clamped at one end containing 8 pairs of piezoelectric patches. The shim has a density of $2700\,\mathrm{kg/m^3}$ and an elastic modulus of $68.9\,\mathrm{Pa}$. PZT-5A piezoelectric unit cells are used for numerical analysis with properties $\bar{c}_{11}^E = 61 \times 10^9\,\mathrm{Pa}$, $\bar{e}_{31} = -12.3\,\mathrm{C/m^2}$, $\bar{\varepsilon}_{33}^S = 13.3 \times 10^{-9}\,\mathrm{F/m}$ and $\rho_p = 7750\,\mathrm{kg/m^3}$. The first piezoelectric element pair nearest to the clamped end of the beam is used as an actuator whereas the remaining seven pairs are shunted to circuits for simultaneous bandgap formation and energy harvesting. We assume that each shunt circuit consists of an inductor and resistor in parallel, corresponding to a normalized admittance of $h(s) = \frac{Y_j(s)}{C_{p,j}} = \frac{\omega_t^2}{s} + \frac{1}{\tau}$ where $\tau = RC_{p,j}$ is the circuit time constant and ω_t is the resonant frequency of the shunt circuit. For large values of τ, the circuit behaves as a purely inductive system, which has been previously discussed in [69]. On the other hand, for small values of τ, the inductor is short-circuited by the resistor.

For given values of τ and ω_t, the beam response and voltage output can be calculated using Equation 3.14 and Equation 3.15. The voltage output can then be used to calculate the real power produced by each piezoelectric unit cell, i.e. $P_j(s) = |V_j(s)|^2/R$, where R is the parallel resistance of the shunt circuit. Here, we use a fixed target frequency of

$\omega_t/(2\pi) = 780\,\mathrm{Hz}$ and vary the value of τ to quantify the power output of the system and the optimal resistive loading conditions.

Figure 3.2 displays the total power output of the beam under voltage excitation (actuation) from the first piezoelectric element at different excitation frequencies and values of τ. It can be seen here that the maximum power of the beam is concentrated near the target frequency immediately before the bandgap. However, it can be observed that as we move further away from the bandgap towards short-circuit conditions, there comes an optimal loading τ_{opt} where maximum power output can be achieved. This optimal loading is shown by the dashed line in the respective Figure.

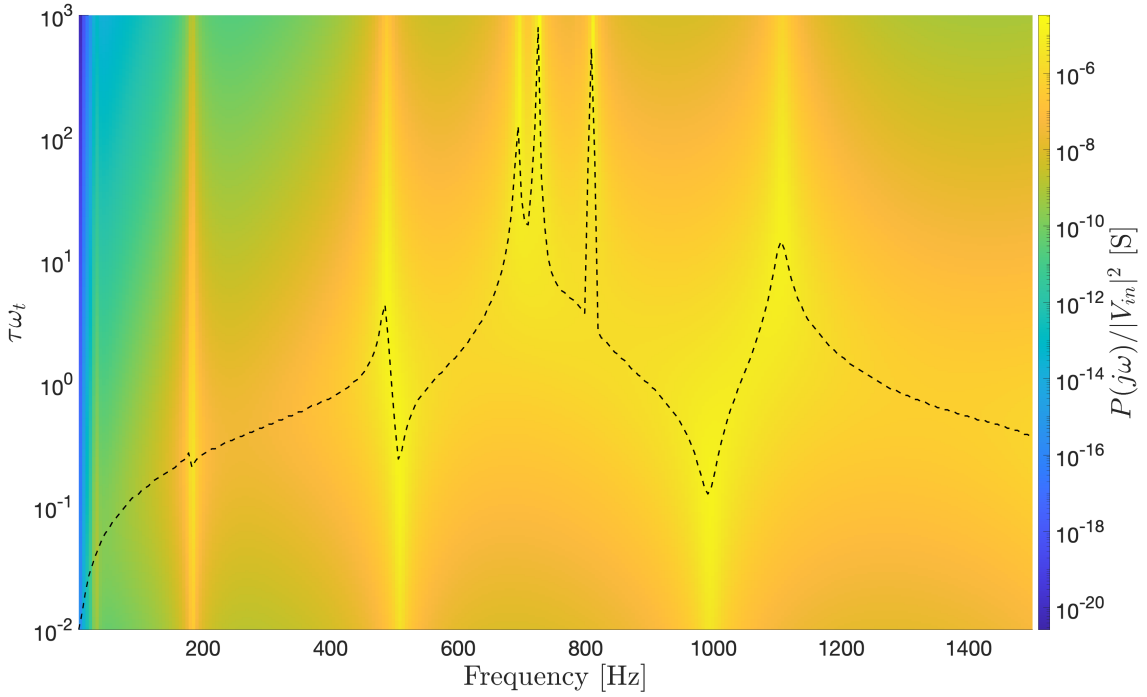

Figure 3.2: Optimal total power output of the electromechanical metastructure as a function of time constant and excitation frequency.

Figure 3.3 shows the beam tip displacement as a function of excitation frequencies and τ. As previously discussed, it can be observed that for large values of τ, the circuit is purely inductive, resulting in a locally resonant bandgap below $780\,\mathrm{Hz}$. However, as the resistance of the circuit is decreased (i.e., as τ is decreased), the width of the bandgap decreases until at one point it vanishes completely. Decreasing this value further fails to obtain the desired

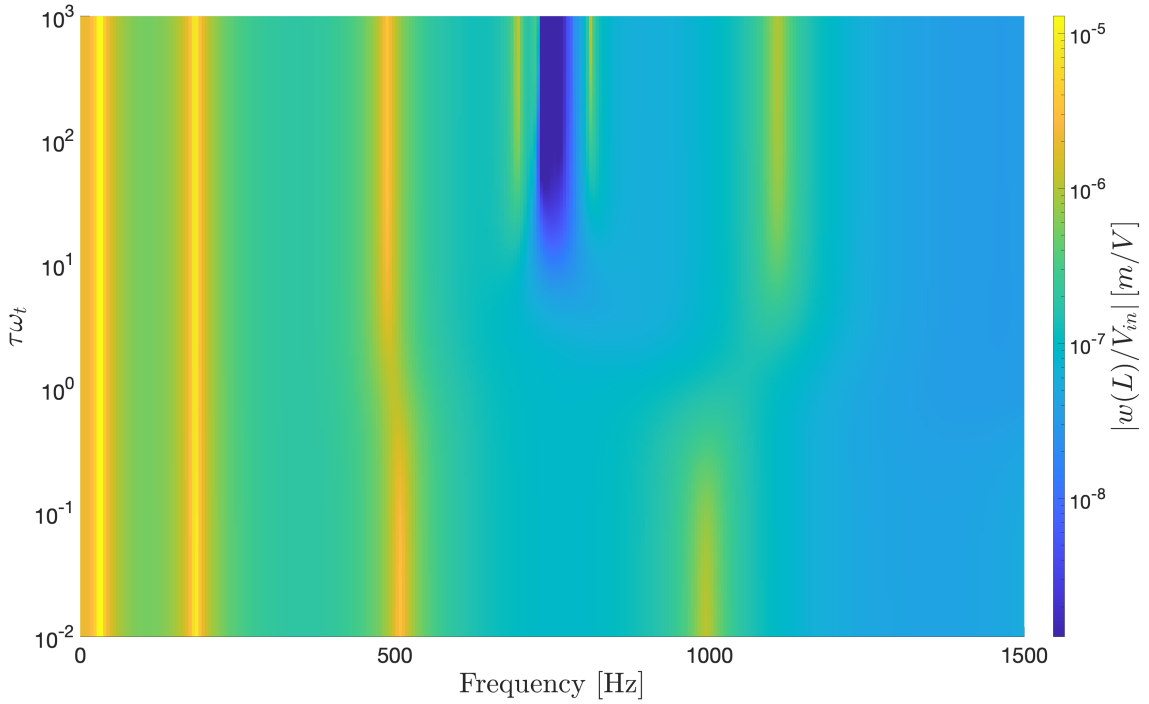

Figure 3.3: Beam tip response for the electromechanical metastructure versus time constant and excitation frequency at the targeted frequency of 780 Hz.

reduction in vibration as the system approaches short-circuit conditions. As a result, there is a trade-off between power output and vibration attenuation, as the bandgap appears only for very large values of τ. To demonstrate this, the displacement of the beam is plotted against frequency for various values of τ in Figure 3.4. It can be seen here that for the maximum value of τ, we obtain a bandgap which disappears as we transition towards lower values i.e. SC conditions.

Power output from the beam and the corresponding beam displacement at optimal value of τ is shown in Figure 3.5 which highlights that at the targeted frequency of 780 Hz, the beam outputs the maximum power (Figure 3.5a) while concurrently also allows for vibration mitigation (Figure 3.5b) at the desired mode. This points at the ideal loading conditions where both attenuation and maximum power output can be achieved together.

In order to understand which piezoelectric unit cells are responsible for generating the most power in the metamaterial beam, we can observe the individual power output for each

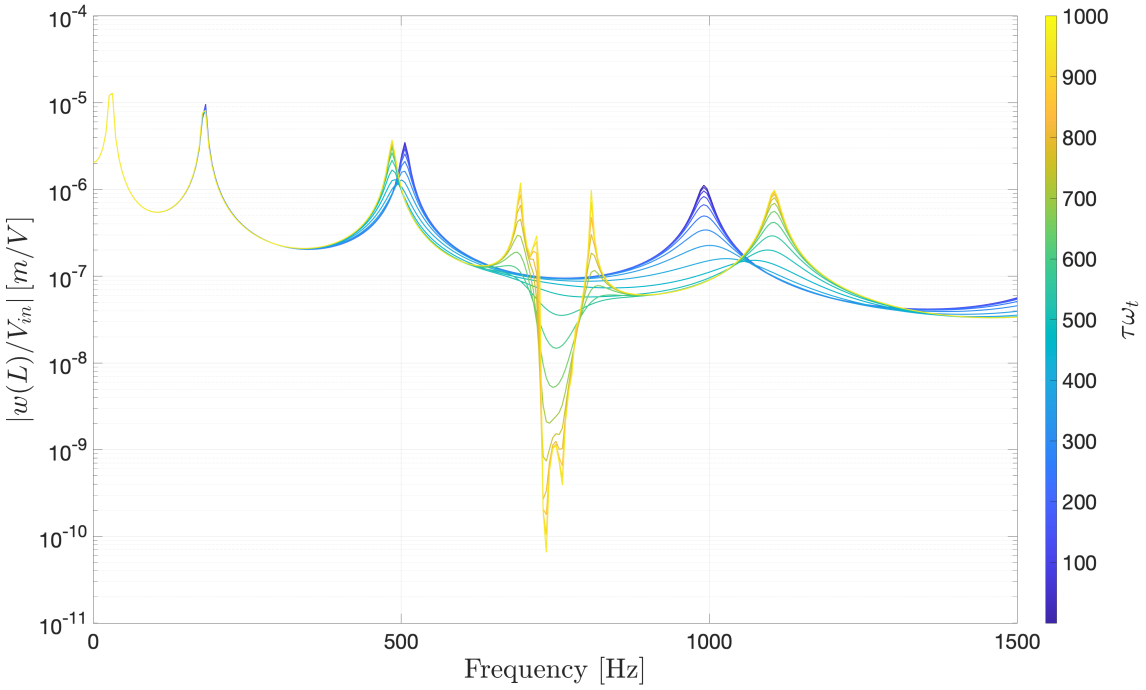

Figure 3.4: Beam tip response versus excitation frequency at different load values.

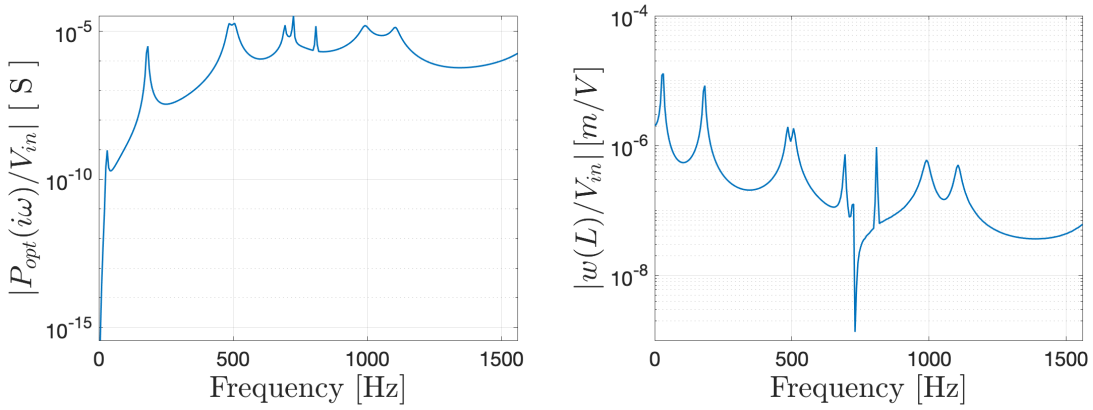

Figure 3.5: (a) Optimal total power output of the electromechanical beam at target frequency of 780 Hz. (b) Beam tip displacement at optimal time constant for the same target frequency.

electromechanical harvester at optimal loading conditions. It can be seen in Figure 3.6a that, as expected, the piezoelectric element nearest to the actuating piezoelectric element outputs the maximum power, and this output reduces as we move towards the tip of the beam. Moreover, each individual piezoelectric patch has the maximum power output im-

mediately before the bandgap at the targeted frequency. Figure 3.6b displays the corresponding percentage optimal power as a function of harvester index. This clearly shows the contribution of each harvester towards the total power extracted from the beam, and it can be observed that the first two harvesters are responsible for 77% and 22% of the total power output.

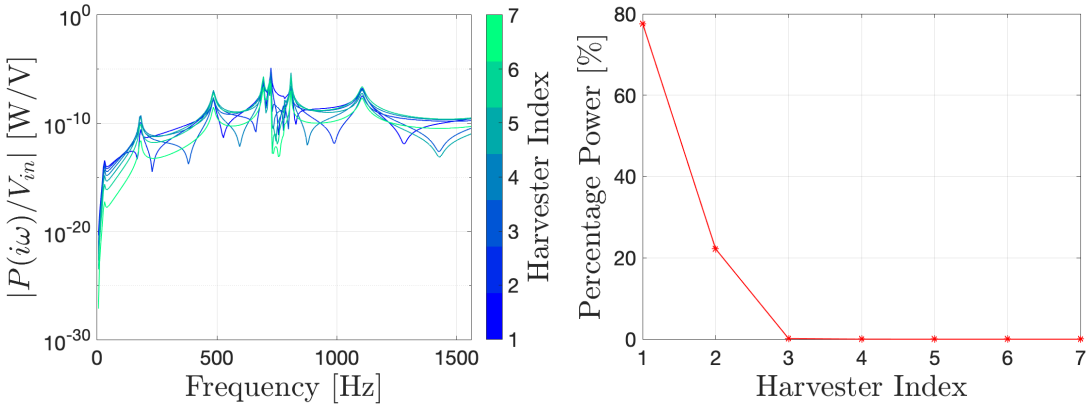

(a) (b)

Figure 3.6: (a) Individual power output of each piezoelectric unit cell at target frequency of 780 Hz. (b) Percentage total power contribution as a function of harvester index.

For the verification of these numerical results, experiments were performed on the beam utilizing the same target frequency ratio to observe the obtained trends experimentally.

3.3 Experimental Results

The experimental setup in Figure 3.7 consists of a main 2024 aluminum beam with 8 pairs of symmetrically bonded PZT-5A patches with dimensions $2.1\,\mathrm{cm} \times 2.1\,\mathrm{cm} \times 0.5\,\mathrm{mm}$ bonded to the main 2024 aluminum beam via an epoxy. Each piezoelectric element is separated by $0.5\,\mathrm{mm}$ to minimize the discrepancy in stiffness between bonded and unbonded areas of the underlying shim. The piezoelectric layers are poled in the same direction through the thickness for parallel-wire operation, and the opposing electrodes are electrically connected. Parallel connection with the shunt circuit is made by properly insulating the central connection and combining the respective electrodes using conductive copper

tape. The piezoelectric element closest to the clamped base is used for beam excitation via voltage actuation, whereas the remaining 7 pairs of piezoelectric unit cells are used for concurrent vibration attenuation and power generation. These piezoelectric elements are shunted to synthetic impedance circuits, which simulate the circuit characteristics of a parallel resistor-inductor (RL) circuit using a voltage-controlled current source and digital controller. The circuits are implemented on a single printed circuit board (PCB) and connected to a controller operating on a NI PXIe-7846R with sample rate 400 kHz. This setup allows digital variation in the inductance and resistance of the shunt circuits to study their effects on the electromechanical LR metastructure. The tip velocity of the beam is measured using a laser Doppler vibrometer (LDV), while the input voltage and the output voltage across each shunted piezoelectric unit cell are recorded simultaneously using the LDV's data acquisition system. The measured capacitance of each shunted piezoelectric segment on the beam is summarized in Table 3.1.

Table 3.1: Capacitance for each piezoelectric patch.

Piezoelectric Patch	Capacitance (C_p) - [F]
1	30.92×10^{-9}
2	31.02×10^{-9}
3	32.02×10^{-9}
4	31.09×10^{-9}
5	31.47×10^{-9}
6	31.29×10^{-9}
7	32.64×10^{-9}

The synthetic impedance circuit in the setup requires a bias resistance $R_b = 1\,\mathrm{M}\Omega$ in parallel to each shunt to pass direct bias current (DC) from the op-amp inputs. Utilizing admittance of the shunt circuitry, total admittance becomes:

$$Y_{j,tot} = C_{p,j}\frac{\omega_t^2}{s} + \frac{C_{p,j}}{\tau} + \frac{1}{R_b} \tag{3.19}$$

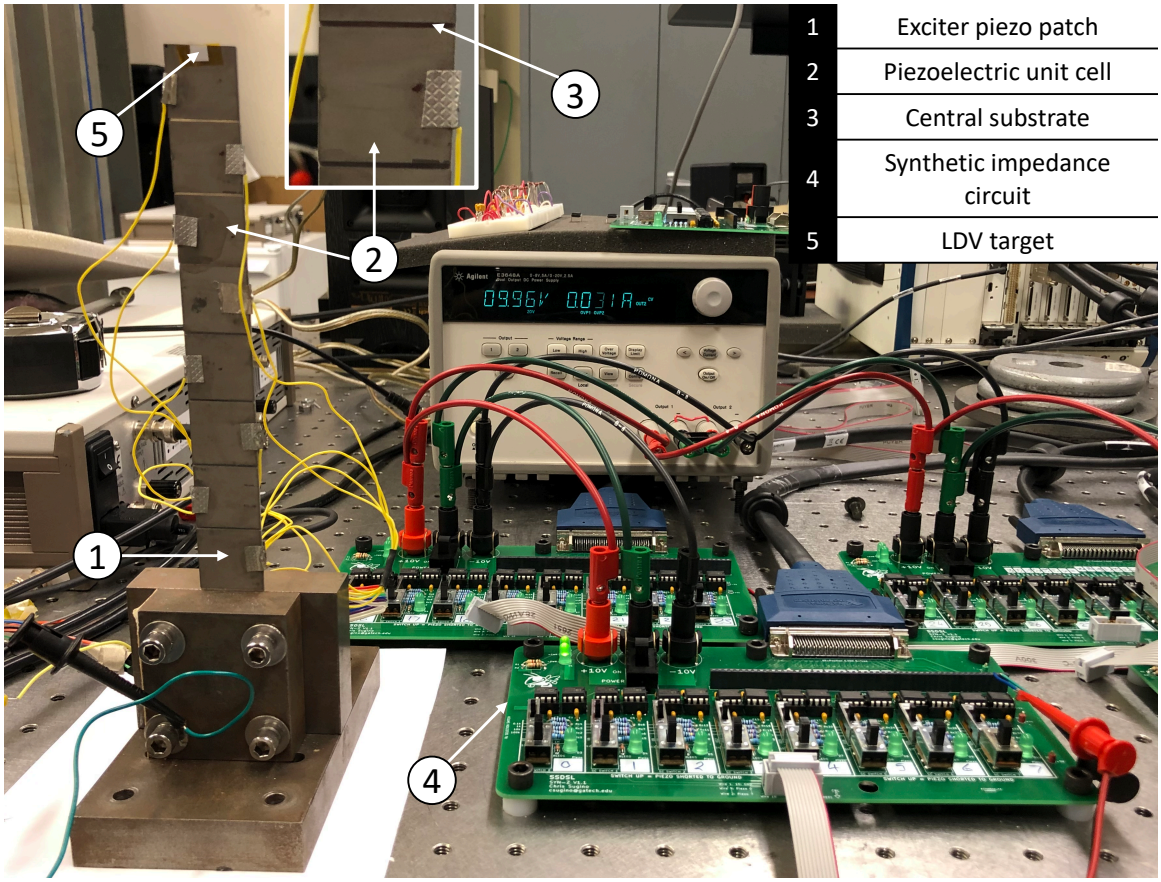

Figure 3.7: Experimental setup for the electromechanical LR metastructure.

Using definition of τ, the total effective resistance for each piezoelectric element can now be written as:

$$R_j = \frac{1}{\left(\frac{C_{p,j}}{\tau} + \frac{1}{R_b}\right)} \tag{3.20}$$

The effective resistance of each shunt is slightly different due to variation in the piezoelectric capacitance $C_{p,j}$, since the target frequency ω_t and time constant τ are kept constant for each shunt. This effective resistance is used in combination with the measured voltage $V_j(\omega)$ across each shunted piezoelectric unit cell to calculate the power produced by the metastructure, i.e. $|P_j(\omega)| = |V_j(\omega)|^2/R_j$. For the experimental results presented here, we use a fixed target frequency of $\omega_t/(2\pi) = 780$ Hz and vary the resistance of the circuit by varying the time constant τ.

Figure 3.8a shows the tip velocity FRF versus time constant and excitation frequency.

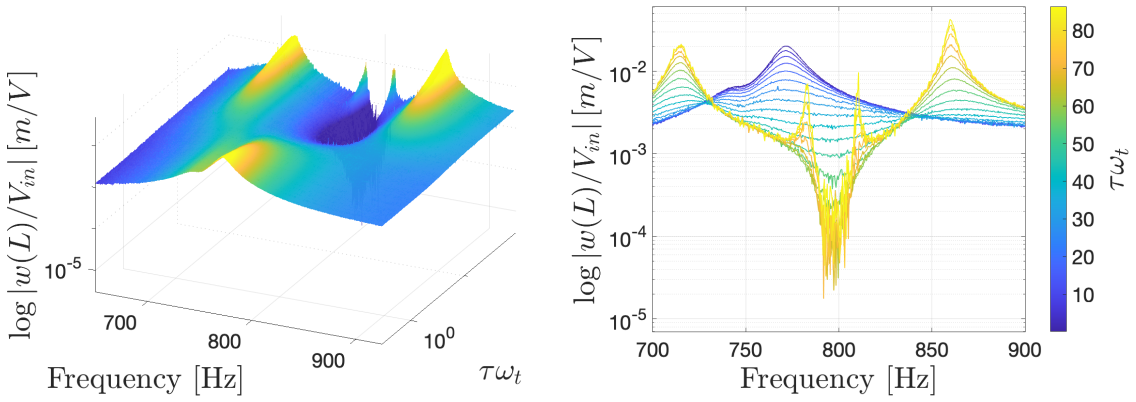

Figure 3.8: (a) Beam tip response for the electromechanical metastructure versus time constant τ and excitation frequency. (b) Beam tip response versus frequency for varying τ.

Under voltage excitation, it can be seen that varying the resistance in the shunt circuit changes the LR bandgap. At $R_p \to \infty$ (open-circuit), the electromechanical metastructure shows the maximum attenuation with a deeper and wider bandgap. On the other hand, as $R_p \to 0$ (short-circuit) the bandgap becomes smaller until it vanishes completely and brings back the original targeted vibration mode. Figure 3.8b shows this more clearly where changes in load resistance directly affects the depth and width of the bandgap, as also portrayed during the numerical analysis.

Total power output from the complete metastructure can be seen in Figure 3.9. At each frequency of excitation, optimal load τ that gives the maximum power output is plotted represented by the dashed line. It can be observed from the figure that as we sweep across load resistances from OC to SC conditions, the corresponding power output around the bandgap neighborhood increases until it reaches a maximum at lower values of τ. Figure 3.8 and Figure 3.9 show that midway between OC and SC conditions, there arises an optimal point where both vibration attenuation and useful power output can be utilized simultaneously since they have opposing trends, similar to what was observed during numerical analysis. The sudden peaks in optimal loading are due to the discretized experimental data especially immediately before each vibration mode.

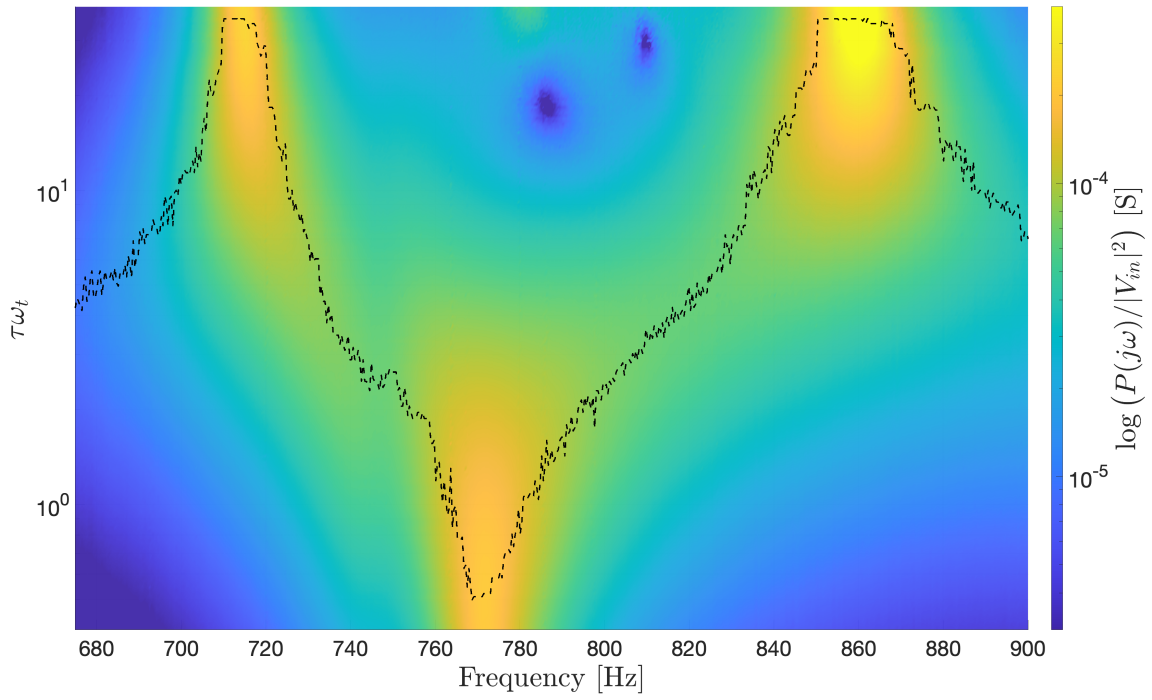

Figure 3.9: Total power output of the complete beam versus time constant and excitation frequency.

The power output of each shunted piezoelectric element is shown in Figure 3.10 as a function of time constant and excitation frequencies. It shows that, for each piezoelectric patch, if we move from the OC conditions towards the SC conditions, power output at the target frequency immediately before the bandgap increases until it arrives at a maximum. As we move along the beam from the actuator piezoelectric segment towards the beam tip, the power output from each element decreases. Thus the maximum power from the beam can be harvested from the first few piezoelectric element pairs with the first and the second harvester responsible for 87% and 11% of the total power output respectively, as shown in Figure 3.11.

Furthermore, the attenuation properties of the beam decrease in the same direction with an increase in power output as analyzed via numerical and experimental analysis. Hence there is a trade-off between the maximum power output and the attenuation capability of the metastructure. Therefore, at an optimal time constant, useful power can be extracted from each piezoelectric unit cell while simultaneous utilization can be made of the vibration

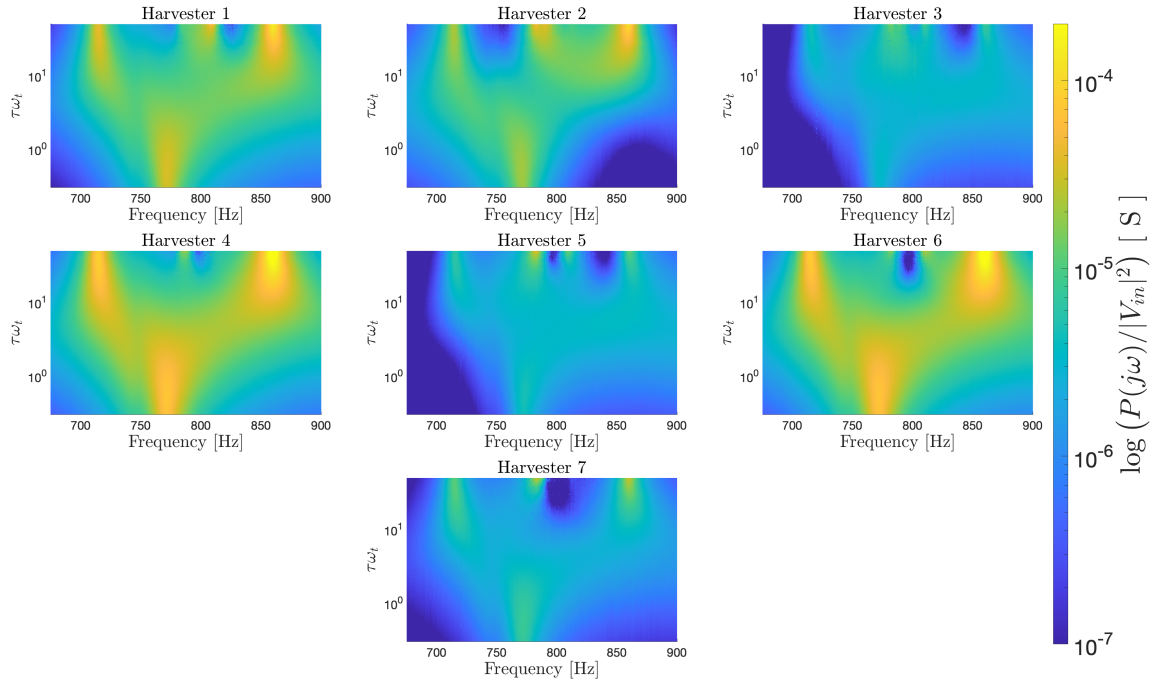

Figure 3.10: Individual power output of each piezoelectric element versus time constant and excitation frequency.

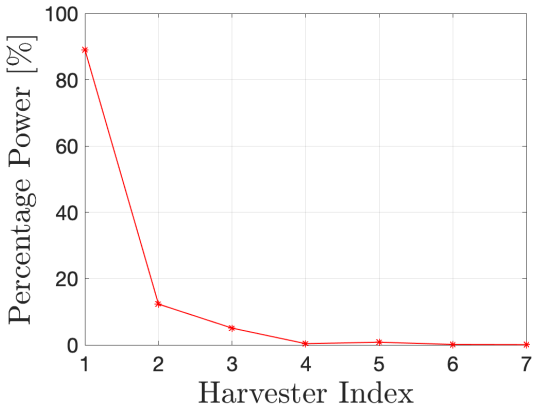

Figure 3.11: Percentage power contribution of each harvester at optimal loading.

attenuation characteristics of the locally resonant electromechanical beam. In addition, the electromechanical metastructure does not require mass additions since the inductors act as resonators. This means that these can be utilized with minimal alterations since the shunt circuitry is always present, and therefore, provides more flexibility towards targeting a variety of vibrational modes and harvesting the desired power.

3.4 Conclusion

Electromechanical locally resonant metastructures make use of synthetic impedance circuits to quantify the electrical voltage outputs and convert them to useful power, but unlike mechanical metastructures, they make use of shunt circuitry to control impedance which is responsible for bandgap formation in such structures. This chapter focuses on numerically and experimentally analyzing the bandgap formation using synthetic shunt circuitry. It evaluates on a framework used to obtain numerical simulations. These simulations show that bandgap in an electromechanical LR metastructure varies with change in resistive loading i.e. τ. A decrease in τ from OC to SC characteristics also reduces the depth and width of the bandgap until it fades away. Simultaneously, an opposing trend can be observed in useful power output where a transition towards SC conditions allow for an increase in power. This analysis displays the existence of an optimal value of shunt loading where both vibration reduction and power harvesting can occur at the same time. This gives rise to a trade-off between vibration attenuation and useful power generation, where both can be targeted at optimal loading only. The same numerical analysis is then verified in the chapter through detailed experimentation. Conventional mechanical resonators make use of the resonance frequency of physical absorbers for bandgap formation and corresponding vibration mitigation which restricts them to a specific target frequency. Their electromechanical counterpart does not only give flexibility of tuning the bandgap, since it depends on the impedance, but also eliminates the requirement of mass addition to the structure. Furthermore, it also allows for greater design flexibility as bandgap can be tuned according to the impedance of the synthetic shunt circuit. Next chapter is aimed towards more non-linear locally resonant metastructures to study the inter dependence of their vibration attenuation and harvesting characteristics as compared to completely linear ones.

CHAPTER 4
NONLINEAR PIEZOELECTRIC ENERGY HARVESTING METASTRUCTURE WITH BISTABLE ATTACHMENTS

So far linear metamaterial beams have been discussed with focus on both mechanical and electromechanical type resonators. This chapter extends the discussion from linear to nonlinear domain detailing the vibration attenuation and energy harvesting capabilities in nonlinear metastructures coupled to bistable attachments, with their tendency to provide subharmonic, superharmonic and chaotic resonance behaviors due to the transient dynamics under a variation of input acceleration levels and corresponding load resistances.

4.1 Nonlinear Energy Harvesting Metastructure

4.1.1 Nonlinear Metastructure Model

The system under consideration consists of a cantilever beam under transverse vibration with S resonators as can be seen in Figure 4.1. The formulation follows the analysis done by Xia et al. [63] and introduces piezoelectric coupling to it in order to harvest energy from the bistable attachments. The main beam is clamped at one end and free to vibrate at the other end. It has a length of L, width of b, thickness of h, Young's modulus of E, and density of ρ. Each resonator is connected to the beam through a nonlinear spring with linear stiffness k_{a1} and cubic stiffness k_{a3}. The total transverse displacement, $w_t(x,t)$, of the jth point on the cantilever beam under base excitation is defined as:

$$w_t(x,t) = w(x,t) + w_b(t) \tag{4.1}$$

where $w_b(t)$ is the base displacement and $w(x,t)$ is the relative displacement of the beam at position x and time t.

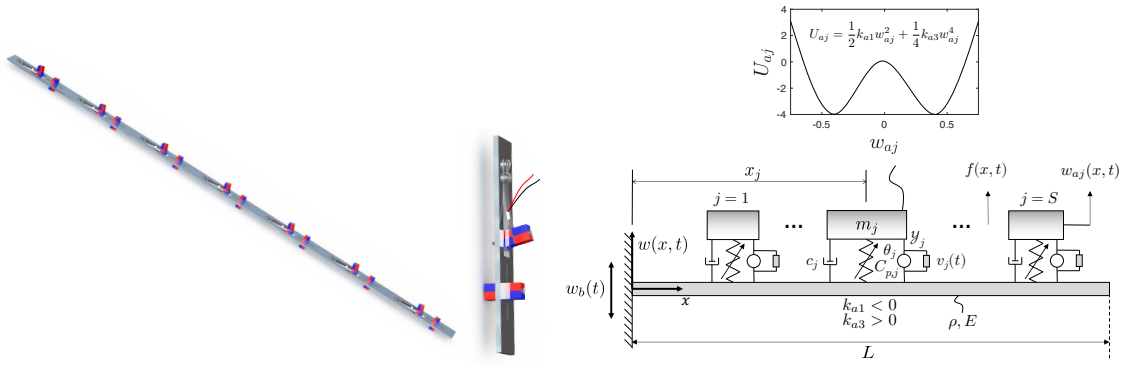

(a) (b)

Figure 4.1: (a) Nonlinear locally resonant metastructure model with bistable cantilever attachments alongside one unit cell. (b) Schematic representation of the nonlinear energy harvesting metastructure with double-well potential of the jth bistable attachment.

For the purpose of this derivation, we will assume the system to be undamped with the knowledge that modal damping can always be introduced later. The governing equation of the main beam is given as:

$$EI\frac{\partial^4 w(x,t)}{\partial x^4} + m\frac{\partial^2 w(x,t)}{\partial t^2} - \sum_{j=1}^{S}\left[k_{a1}w_{aj}(t) + k_{a3}w_{aj}^3(t)\right]\delta(x-x_j) = -m\frac{d^2 w_b(t)}{dt^2} \tag{4.2}$$

with associated equations for the corresponding resonators:

$$m_j\left[\frac{\partial^2 w(x_j,t)}{\partial t^2} + \frac{d^2 w_{aj}(t)}{dt^2}\right] + k_{a1}w_{aj}(t) + k_{a3}w_{aj}^3(t) - \vartheta_j v_j = -m_j\frac{d^2 w_b(t)}{dt^2}, \qquad j = 1...S \tag{4.3}$$

$$C_{p,j}\dot{v}_j + \mathscr{Y}_j[v_j] + \vartheta\dot{u}_j = 0, \qquad j = 1...S \tag{4.4}$$

where $w_{aj}(t)$ is the relative displacement of the jth resonator with respect to $w(x_j,t)$, x_j is the location of the jth resonator, $m = \rho bh$ is the mass per length of the beam, m_j is the mass of the jth resonator, ϑ_j,$C_{p,j}$, and $\mathscr{Y}_j$ are the electromechanical coupling, effective

piezoelectric capacitance, and admittance operator of the shunt circuit on the jth resonator. The boundary conditions of the clamped-free beam are:

$$w(0,t) = 0, \qquad \frac{\partial w(0,t)}{\partial x} = 0, \tag{4.5}$$

$$EI\frac{\partial^2 w(L,t)}{\partial x^2} = 0, \qquad EI\frac{\partial^3 w(L,t)}{\partial x^3} = 0 \tag{4.6}$$

Even though the mode shapes of a clamped-free beam are not the exact mode shapes of the whole system because the force exerted by the resonators depends on the displacement of the beam, an expansion using the mode shapes of the clamped-free beam, $\phi(x)$, can provide significant simplification. The approximate solution is considered in the form as follows:

$$w(x,t) = \sum_{r=1}^{N} \eta_r(t)\phi_r(x) \tag{4.7}$$

where N is the number of modes in the expansion, and $\eta_r(t)$ is the modal weighting of the rth mode of the clamped-free beam. The mass-normalized mode shapes of the beam are:

$$\phi_r(x) = \frac{1}{\sqrt{mL}}\Bigg[\cos\left(\frac{\lambda_r x}{L}\right) - \cosh\left(\frac{\lambda_r x}{L}\right) + \left(\frac{\sin\lambda_r - \sinh\lambda_r}{\cos\lambda_r + \cosh\lambda_r}\right)\left(\sin\left(\frac{\lambda_r x}{L}\right) - \sinh\left(\frac{\lambda_r x}{L}\right)\right)\Bigg], \qquad r = 1...N \tag{4.8}$$

where λ_r is the rth positive real solution of the characteristic equation:

$$\cos\lambda\cosh\lambda + 1 = 0 \tag{4.9}$$

Substituting Equation 4.7 into Equation 4.2, we have:

$$EI\sum_{r=1}^{N}\eta_r(t)\phi_r''''(x) + m\sum_{r=1}^{N}\ddot{\eta}_r(t)\phi_r(x) - \sum_{j=1}^{S}\left[k_{a1}w_{aj}(t) + k_{a3}w_{aj}^3(t)\right]\delta(x - x_j) = -m\ddot{w}_b(t) \tag{4.10}$$

Multiplying Equation 4.10 by $\phi_s(x)$, integrating from $x = 0$ to $x = L$, and applying the orthogonality conditions of the mode shapes gives:

$$\ddot{\eta}_r(t) + \omega_r^2 \eta_r(t) - \sum_{j=1}^{S} \left[k_{a1} w_{aj}(t) + k_{a3} w_{aj}^3(t)\right] \phi_r(x_j) = -m\ddot{w}_b(t) \int_{x=0}^{x=L} \phi_r(x) dx \tag{4.11}$$

By substituting Equation 4.7 into Equation 4.3, we get the following Equation:

$$m_j \left[\sum_{r=1}^{N} \ddot{\eta}_r(t) \phi_r(x_j) + \ddot{w}_{aj}(t) \right] + k_{a1} w_{aj}(t) + k_{a3} w_{aj}^3(t) - \vartheta_j v_j = -m_j \ddot{w}_b(t), \qquad j = 1...S \tag{4.12}$$

In order to make the governing equations coupled through inertial terms only, we can rewrite Equation 4.11 by substituting Equation 4.12 as:

$$\ddot{\eta}_r(t) + \omega_r^2 \eta_r(t) - \sum_{j=1}^{S} \vartheta_j v_j \phi_r(x_j) + \sum_{j=1}^{S} m_j \phi_r(x_j) \sum_{k=1}^{N} \ddot{\eta}_k(t) \phi_k(x_j) + \sum_{j=1}^{S} m_j \ddot{w}_{aj}(t) \phi_r(x_j) = q_r(t), \qquad r = 1...N \tag{4.13}$$

where

$$q_r(t) = -\ddot{w}_b(t) \left(\int_{x=0}^{x=L} m \phi_r(x) dx + \sum_{j=1}^{S} m_j \phi_r(x_j) \right) \tag{4.14}$$

Equation 4.12, Equation 4.13 and Equation 4.4 form a system of $N + 2S$ coupled second order ordinary differential equations. The system can be put into the matrix form as below:

$$\mathbf{M\ddot{u}} + \mathbf{C\dot{u}} + \mathbf{Ku} + \mathbf{Gu^3} = \mathbf{F}(t), \tag{4.15}$$

Rest of the procedure is similar to the analysis done by Xia et al. [63] in order to solve this matrix further to get the desired system of equations. These are utilized in the next section

in order to obtain numerical simulations for the aforementioned system model.

4.2 Numerical Results

This section focuses on numerical analysis of the system described in Figure 4.1. It explores the broadband dynamic behavior of nonlinear bistable resonators by analyzing their effect on transmissibility and power output of the individual harvesters, and the beam as a whole. Parameters used for this analysis are based on the practical experimental setup described in the next section, and adjusted accordingly. These can be seen in Table 4.1. The analysis here targets the second vibration mode [63] ($15.9\,\mathrm{Hz}$) of the clamped-free cantilever beam with additional masses, at a target frequency of $w_t/(2\pi) = 17\,\mathrm{Hz}$. Adjusted thickness and density values are used for numerical investigation since it accounts for the variation in experimental setup pertaining to extrusion of holes, slots, added masses, etc. This is a relatively reasonable approach due to long wavelength around the target frequency compared to dimensions of such components. Modal damping is incorporated in both the beam and the bistable resonators (Equation 4.12 and Equation 4.13), as mentioned in Table 4.1. Some important assumptions made for the analysis are as follows:

- The mass of each resonator is assumed to be the same throughout the beam.
- All springs used in the model have the same stiffness.
- Modal damping for all bistable attachments is assumed to be identical.

As nonlinear system responses are dependent upon acceleration levels of the base excitation, the system under consideration was studied numerically under three cases of base acceleration: $0.05g$, $0.1g$ and $0.15g$ (RMS values) where g denotes gravitational acceleration. Up and down frequency sweeps were performed over the frequency range of $10\,\mathrm{Hz}$-$24\,\mathrm{Hz}$ for the respective FRF simulations. All the bistable attachments are assumed to start from positive equilibrium position while the beam starts to move from rest.

Table 4.1: Beam parameters for the nonlinear metastructure.

Length of the beam (L)	$0.889\,\mathrm{m}$
Width of the beam (b)	$0.031\,75\,\mathrm{m}$
Thickness of the beam (h)	$0.003\,175\,\mathrm{m}$
Spring steel cantilever length (l_a)	$0.0406\,\mathrm{m}$
Spring steel cantilever width (b_a)	$0.009\,525\,\mathrm{m}$
Spring steel cantilever thickness (h_a)	$0.000\,254\,\mathrm{m}$
Dimensions of cube shaped magnets ($l \times b \times h$)	$0.009\,525\,\mathrm{m}$
Adjusted beam thickness (h_a)	$0.0026\,\mathrm{m}$
Young's modulus (E)	$69 \times 10^9\,\mathrm{Pa}$
Density (ρ)	$2700\,\mathrm{kg/m^3}$
Adjusted density (ρ_a)	$2970\,\mathrm{kg/m^3}$
Tip mass (m_r)	$0.0036\,\mathrm{kg}$
Bistable equilibrium positions (w_a)	$\pm 0.75\,\mathrm{cm}$
Spring linear stiffness (k_{a1})	-63.451 $\mathrm{N/m}$
Spring cubic stiffness (k_{a3})	$634\,509\,\mathrm{N/m^3}$
Modal damping ratio of the beam (ζ_b)	0.002
Damping ratio of the attachments (ζ_a)	0.02
Number of modes (N)	10
Number of unit cells (S)	7
Load resistances (R_l)	$887\,\mathrm{k\Omega}$, $2.74\,\mathrm{M\Omega}$, $8.87\,\mathrm{M\Omega}$

The simulated transmissibility response for the beam is shown in Figure 4.2 for various excitation levels and load resistances with the linear bandgap as a reference, for both up and down frequency sweeps. It can be observed that for lower values of acceleration, bistable attachments oscillate around their initial equilibrium positions at their natural resonant frequency. This is associated with the linear\quasilinear behavior of the attachments which is similar to the conventional linear behavior of the beam. A typical LR bandgap can be seen where the targeted mode is attenuated while additional resonances appear on either side of the bandgap. As this acceleration level is increased, we can see nonlinear oscillations of the

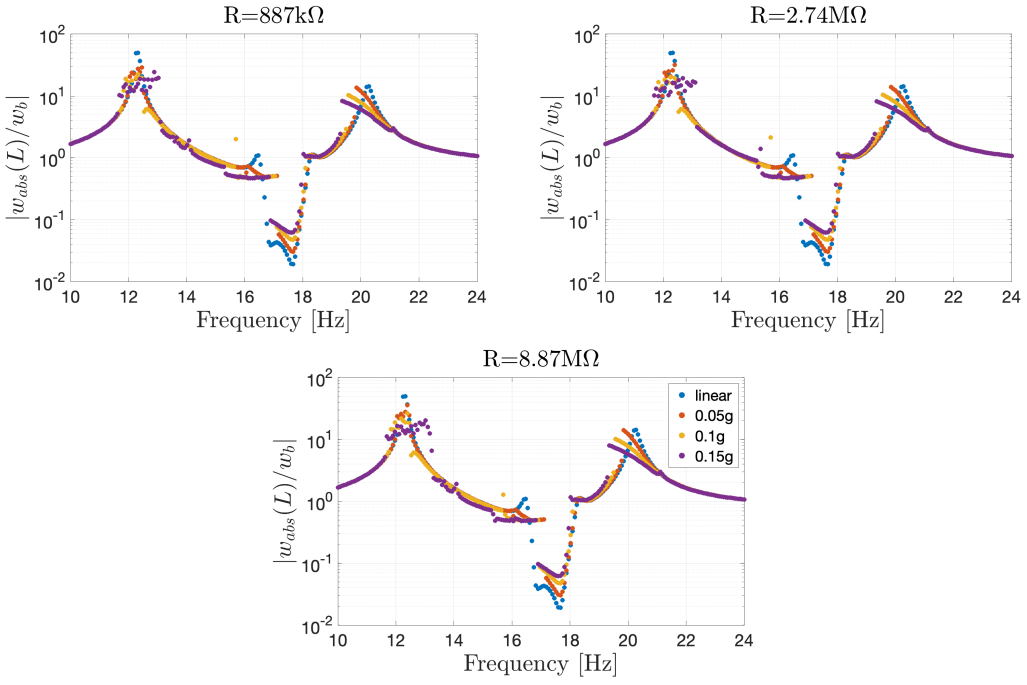

(a)

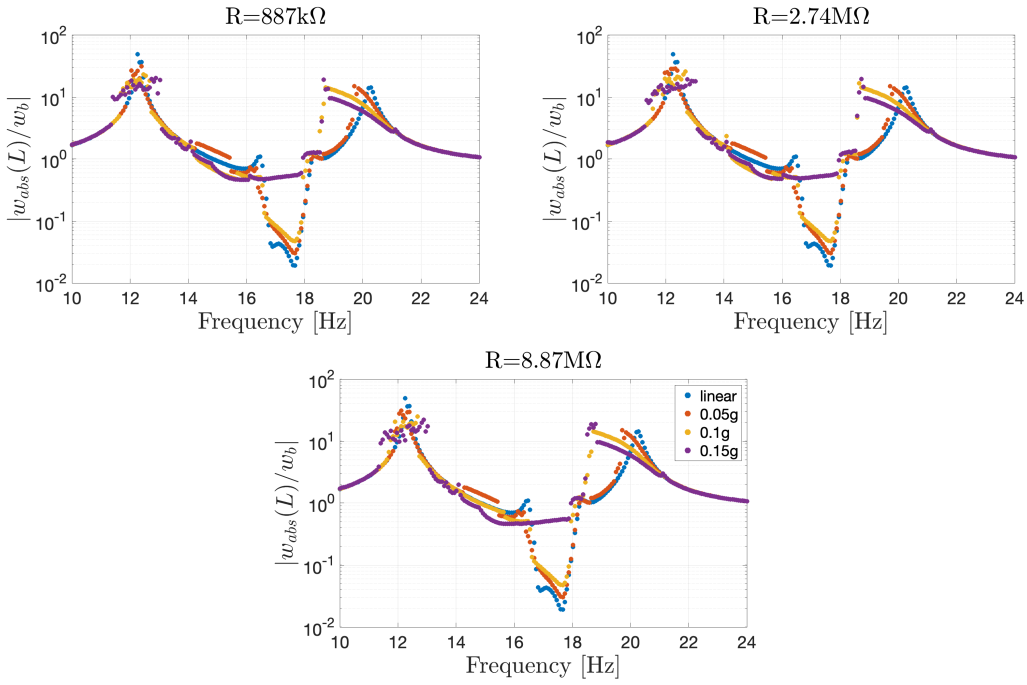

(b)

Figure 4.2: Simulated frequency response for the transmissibility of the beam under various base excitation levels: (a) Up sweep. (b) Down sweep.

bistable attachments due to which, broadband attenuation can be observed. At the chaotic frequency region of $12.1\,\mathrm{Hz}$, gradual mitigation of the vibration mode can be noticed i.e. enhanced attenuation due to a broader bandwidth. As can be seen for both up and down sweeps, the bandgap becomes less deep but wider with an increase in acceleration level. This behavior can be observed for all load resistances.

In order to observe the power output behavior from each piezoelectric unit cell at various acceleration levels, Figure 4.3 displays the respected power generated for both up and down sweeps at load resistance of $2.74\,\mathrm{M\Omega}$. For the sake of convenience and brevity, results for only one load resistance is shown here. Similar to the linear beam with resonator case, a decreasing trend can be observed at the target frequency of $17\,\mathrm{Hz}$ as we move from the first piezoelectric unit cell towards the last one where the first harvester outputs the maximum power. If we look at the lowest acceleration level of $0.05g$, the power output behavior is similar to the linear case at the target frequency. However with increasing acceleration levels, as interwell oscillations start to take place, wideband chaotic behavior initiates which allows for useful power generation at a wider range of frequencies than its linear counterpart. Furthermore, this oscillatory action also helps in harvesting useful power from the chaotic region at $12.1\,\mathrm{Hz}$ where the range of frequencies for power harnessing is broader in comparison to power output from attachments at lower acceleration values. Observing the different harvesters, it can be seen that even though power output at the target frequency neighborhood is minimal for the 7th piezoelectric element, it can still output useful power at the chaotic frequency region. This can be said for other unit cells as well where useful power generation in the chaotic neighborhood does not follow the conventional decreasing trend as we move across the fixed to free end of the beam. Hence, this behavior associated with bistable energy harvesting attachments provides an advantage over orthodox beams with linear resonators. The same reaction can be observed at load values of $887\,\mathrm{k\Omega}$ and $8.87\,\mathrm{M\Omega}$, where most of the power can be harnessed from optimal loading of $2.74\,\mathrm{M\Omega}$.

Figure 4.4 displays the total power output of the complete beam at different accelera-

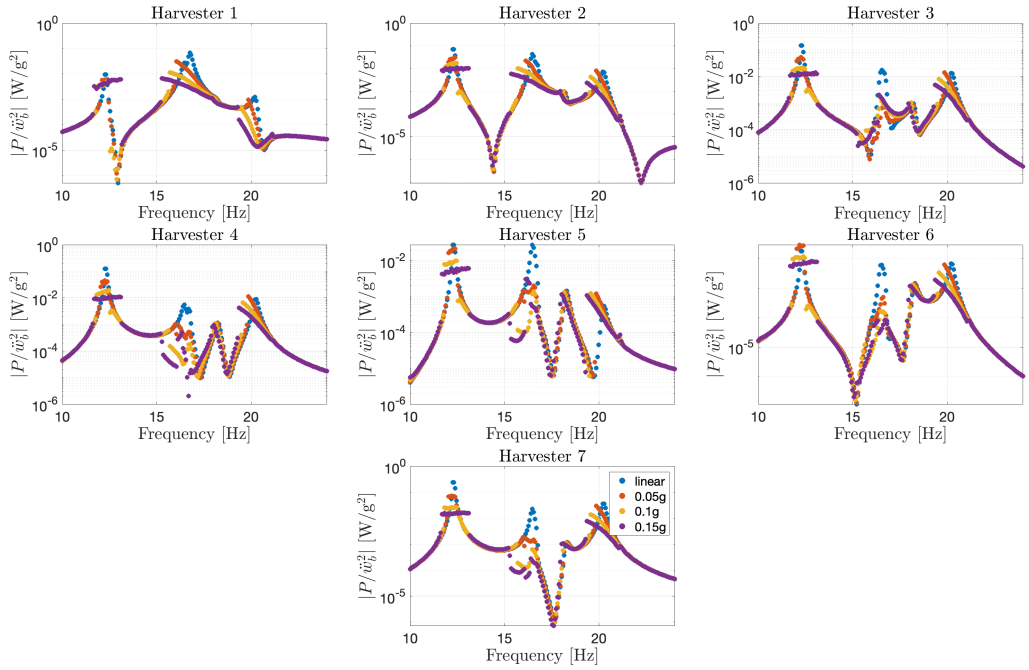

(a)

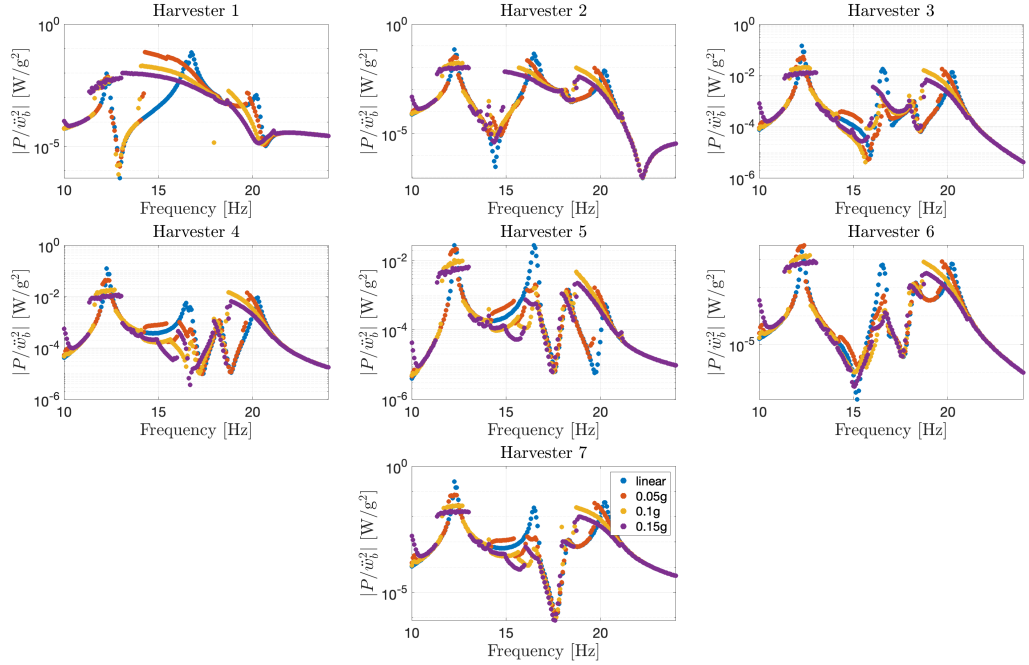

(b)

Figure 4.3: Simulated individual power output from each harvester at various acceleration levels at $R = 2.74M\Omega$ and $\omega_t/(2\pi) = 17\,\text{Hz}$: (a) Up sweep. (b) Down sweep.

tion levels for both up and down sweeps. It can be observed that at the target frequency of $17\,\text{Hz}$ in the bandgap neighborhood, total power output decreases as we move from lower

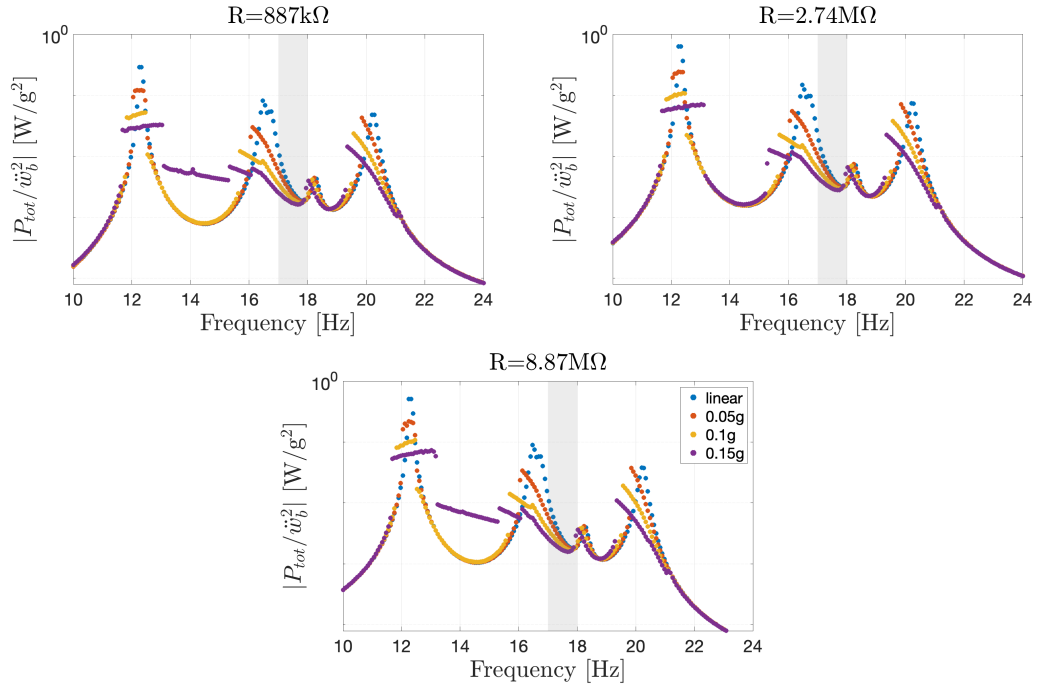

(a)

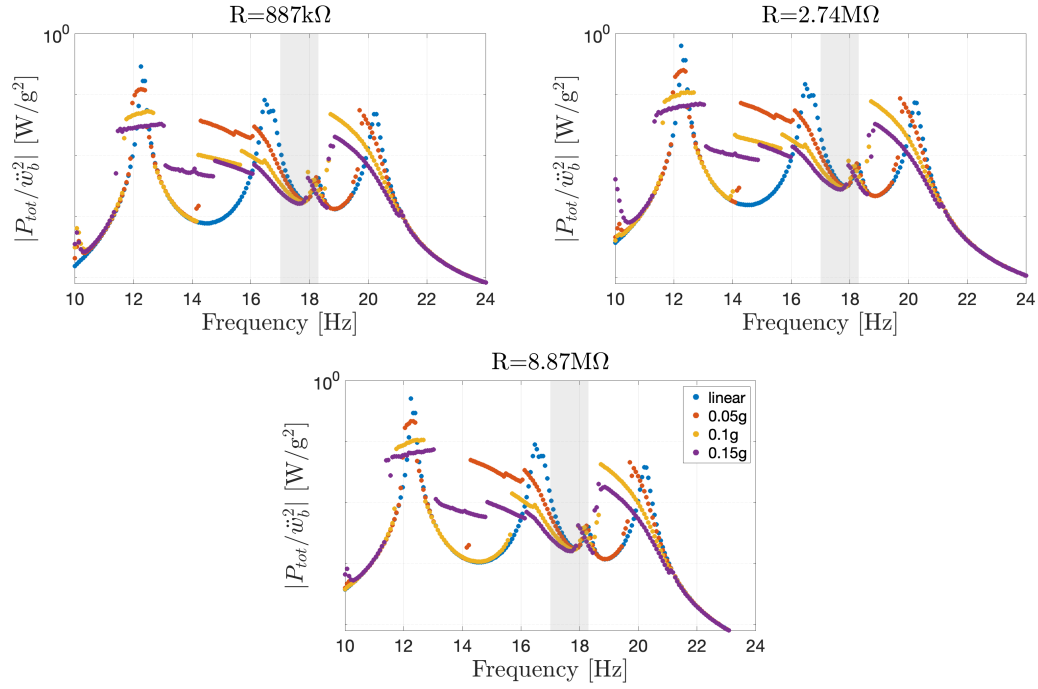

(b)

Figure 4.4: Simulated total power output of the complete nonlinear metastructure around the bandgap neighborhood displayed by the grey region: (a) Up sweep. (b) Down sweep.

acceleration levels to higher ones. However, the chaotic wideband oscillations allow for an enhanced frequency range from where power can be harvested around the bandgap. Interestingly, maximum total power can be harnessed at chaotic frequency of $12.1\,\mathrm{Hz}$ where the highest acceleration level of $0.15g$ provides a much broader range of frequencies to harvest power from the beam, in comparison to other excitation levels. Therefore, even though an increase in base excitation amplitude widens the bandgap and provides transmissibility suppression for neighboring vibration modes as well, it simultaneously brings forth an opportunity to harvest power from neighboring chaotic frequency ranges, unlike linear beams. This can be observed for all load values.

Percentage power contribution in Figure 4.5 shows that for different excitation levels, the first few harvesters output the maximum power. The first two piezoelectric unit cells are responsible for 84% and 14% of the total power output for the linear case. Percentage power contribution for the first harvester decreases with an increase in excitation levels. However, the contributions from the other unit cells increase due to a wider range of frequencies where power can be harnessed under chaotic wideband behavior of bistable oscillators for example, for $R = 2.74\,\mathrm{M}\Omega$ at $0.15g$, 53%, 32% and 12% of the total power is generated by the first three resonators respectively. Therefore, in comparison to the linear case, useful power output can be generated and utilized up until the third unit cell where total power contribution is spread out among the first few resonators, and similar trend can be seen for all load values. Hence, interwell oscillations of the bistable nonlinear resonators not only allow for enhanced vibration attenuation but also provide an increased range of frequencies for power generation. This behavior is experimentally verified in the next section for the same acceleration levels and beam parameters.

4.3 Experimental Results

The experimental setup consists of a main central aluminum beam structure with 7 small spring steel cantilever attachments, as shown in Figure 4.6. Each of these unit cells fur-

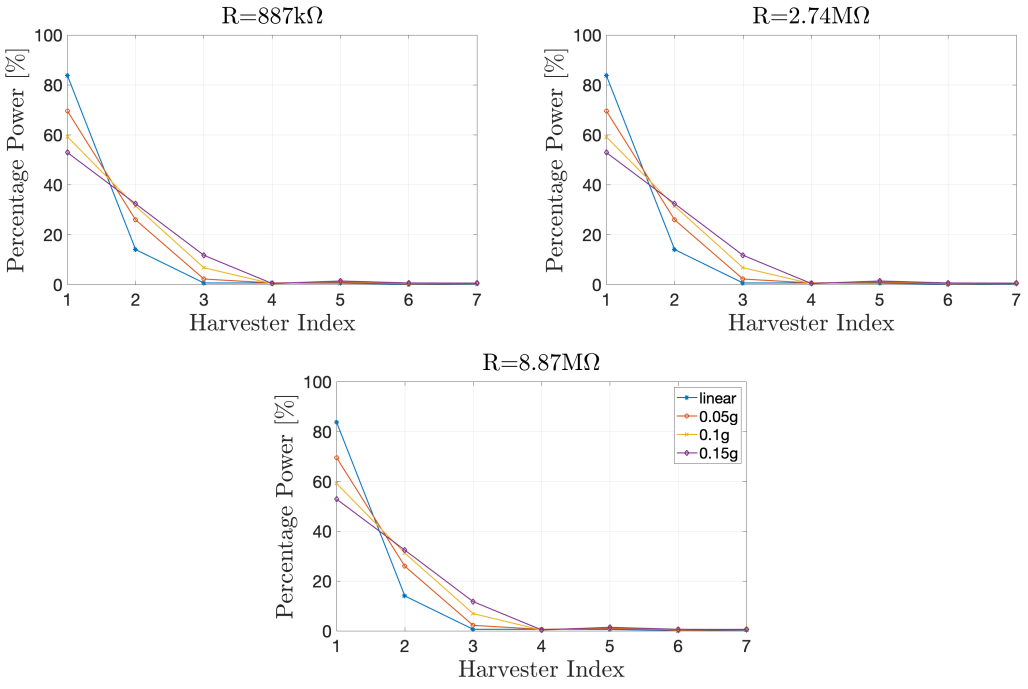

(a)

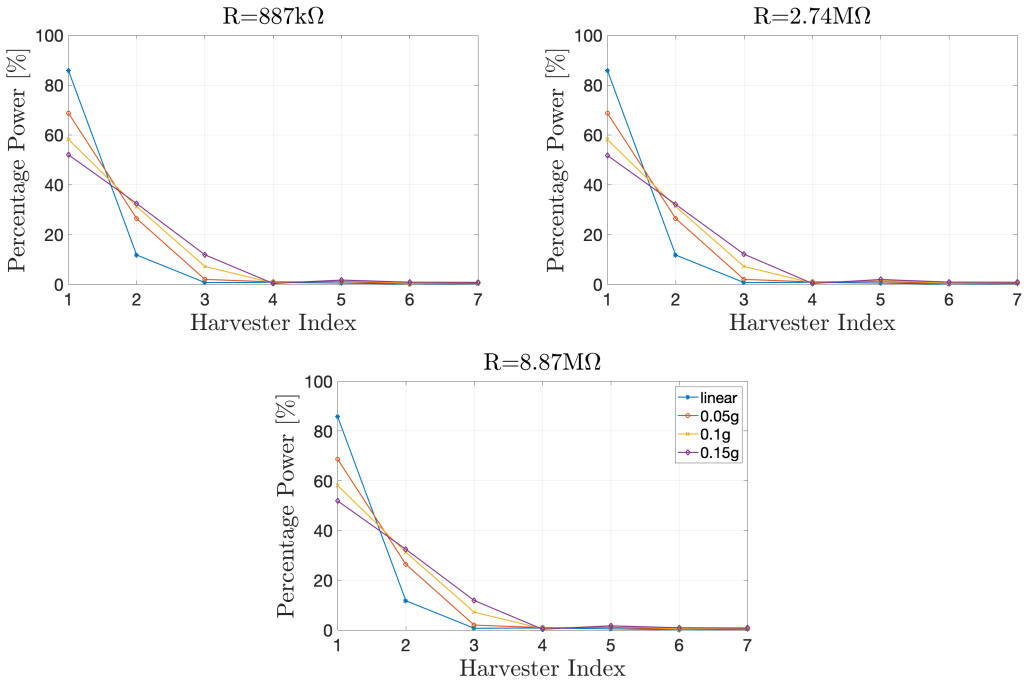

(b)

Figure 4.5: Percentage power contribution for the simulations as a function of harvester index at different excitation levels: (a) Up sweep. (b) Down sweep.

ther has a pair of $9.525\,\mathrm{mm} \times 9.525\,\mathrm{mm}$ permanent magnets fixed at the end via a bolt, which remains perpendicular to the direction of magnetization. Another pair of the same permanent magnets identical in dimensions to the previous one is fixed on the main beam in a slot at a distance of $17\,\mathrm{mm}$ measured from the edge of the previous magnets. These help in obtaining the bistable equilibrium positions for the magnetoelastic cantilever beam attachments. An APS-400 shaker is used to excite the main structure (via base excitation) at 3 different acceleration levels which is clamped to the armature of the shaker. This acceleration is measured using an accelerometer fixed at the base of the beam. A controller is used to ensure harmonic base acceleration at constant amplitudes and specified frequencies. These frequencies are swept up and down from $10\,\mathrm{Hz}$ to $24\,\mathrm{Hz}$ at a rate of $0.25\,\mathrm{Hz/min}$. Due to practical constraints, $9.525\,\mathrm{mm} \times 9.525\,\mathrm{mm}$ piezoelectric patches are placed at the center of each cantilever attachment, instead of at the base, connected to electrical loads in order to quantify voltage output from these bistable unit cells. At the base of each cantilever spring steel, strain becomes large enough which starts to crack the piezoelectric unit cells; or the vibrations in the chaotic region cause the wires to break off. Resistance sweep is performed at a particular value of acceleration for 3 different load resistances. A Polytec OFV-505 LDV is used to measure the tip velocity of the beam. Beam parameters can be seen in Table 4.1.

The bistable attachments consist of potential wells which can be tweaked by changing the distance (d) between magnets on the beam, and on the spring steel cantilever. For the purpose of this experiment, $d = 17\,\mathrm{mm}$ is used which provides a post-buckled natural frequency of $17\,\mathrm{Hz}$ in order to target the second mode of the beam. All the bistable attachments start from their positive equilibrium positions while the beam is at rest. A linear experiment is performed initially with the attachments to act as a reference. Experiments are conducted afterwards for 3 different base excitation levels identical to the ones used in numerical simulations.

Figure 4.8 shows the experimentally obtained beam tip displacement normalized by

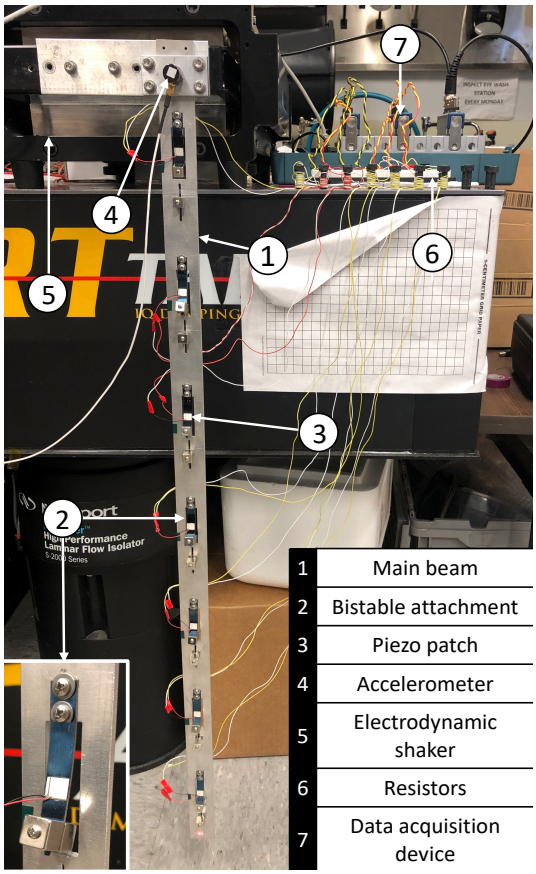

Figure 4.6: Experimental setup consisting of the main beam with seven bistable attachments connected to electrical loads

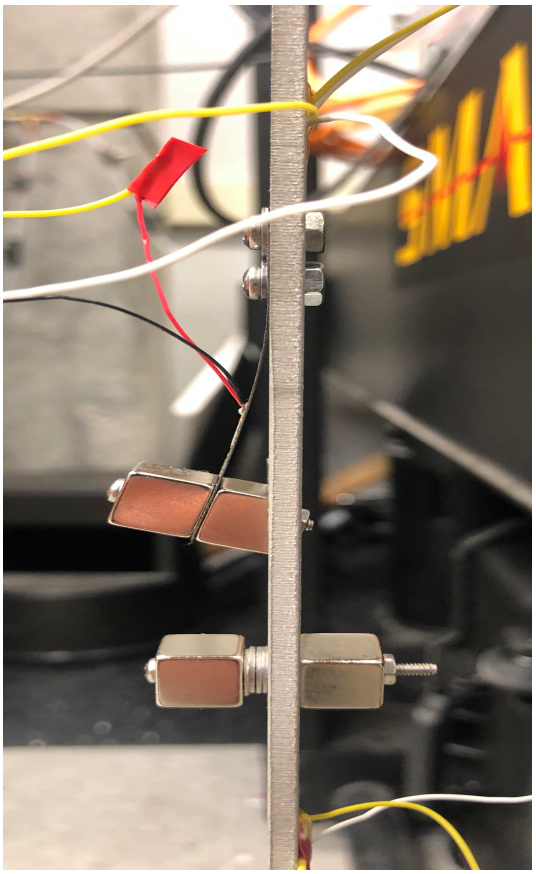

Figure 4.7: Side view of a single bistable unit cell

base acceleration, for different excitation levels. In comparison to Figure 4.2, it can be observed that the experimental results agree well with the numerically simulated data. At lower values of acceleration i.e. $0.05g$, the bistable attachments remain in their potential wells to maintain their respective stable equilibrium positions. Hence the vibration is linear or quasilinear like the conventional LR bandgap obtained from linear metastuctures. Additional resonances appear on either side of the attenuated mode and a bandgap is formed. Higher g values of acceleration effect the width and depth of the attenuation band due to nonlinear wideband attenuation. The chaotic motion of the bistable attachments between its equilibrium positions causes this enhanced frequency attenuation. It can be seen that, at greater excitation levels, the bandgap becomes wider, however the depth lessens. For

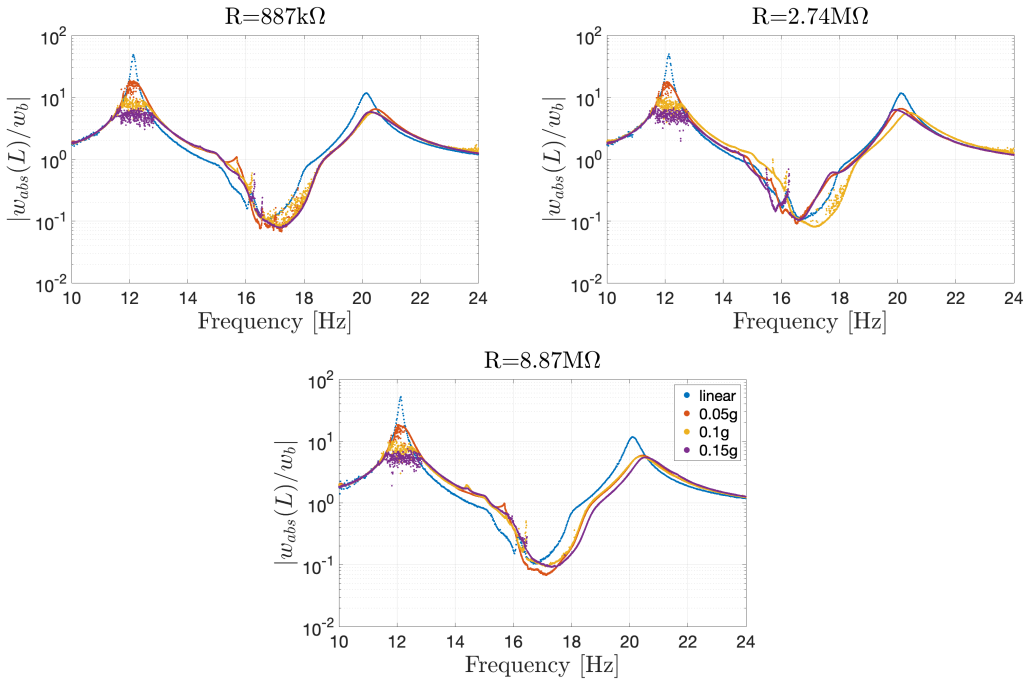

(a)

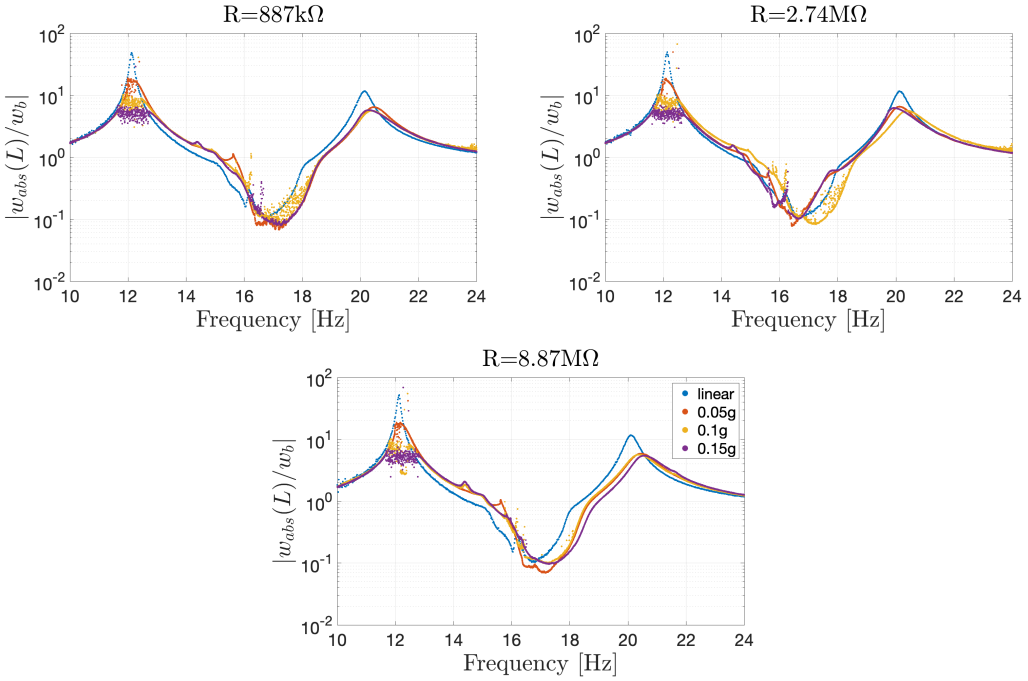

(b)

Figure 4.8: Experimental FRF response for the transmissibility of the beam under various base excitation levels: (a) Up sweep. (b) Down sweep.

$R = 2.74\,\mathrm{M}\Omega$ at 0.15g, a 116.67% increase can be observed in attenuation frequency range as compared to the linear case. Similarly the depth of the attenuation band decreased by 21.67%. This is a direct effect of the attachments' nonlinear dynamics and also caters to additional modes for attenuation. Similar trend can be seen for all load resistances.

Individual power output for each piezoelectric unit cell can be seen in Figure 4.9. Again, for ease of comparison, only loading resistance of $R = 2.74\,\mathrm{M}\Omega$ is shown here. Just like in the simulations, maximum power output at the target frequency of $17\,\mathrm{Hz}$ is obtained from the first piezoelectric element which decreases as we move towards the last one. Additionally, at this frequency, the power output decreases with an increase in acceleration level. However, unlike the linear case, the increase in base excitation allows for chaotic regions, for example, around $12.25\,\mathrm{Hz}$ in this case due to the interwell oscillatory nature of bistable attachments. As can be seen in the figure, this provides an enhanced frequency range from where power can be harnessed and includes the chaotic frequency range. For each piezoelectric unit cell, even though the power output at the target frequency decreases, it can still be harvested from the chaotic region. Therefore, all of the piezoelectric elements can be utilized to harness useful power around the chaotic frequency. This result agrees with the numerical analysis from the previous section and displays the same tendency for other load values.

The total power output from the complete metastructure can be seen in Figure 4.10 for different g values. For all load resistances, it can be observed that the total power generated by the complete metastructure around the bandgap neighborhood is maximum for the linear case and decreases with an increase in acceleration level, which is as expected from the simulations. After initiation of nonlinear chaotic oscillations of bistable resonators, broadband attenuation takes place which enhances the frequency range from where power can be harnessed. Around the chaotic frequency of $12.25\,\mathrm{Hz}$, it can be seen that for an increase in base excitation, the range of frequency increases. This allows for maximum total power output from the structure over a wide range of frequencies. Hence, alongside a broader

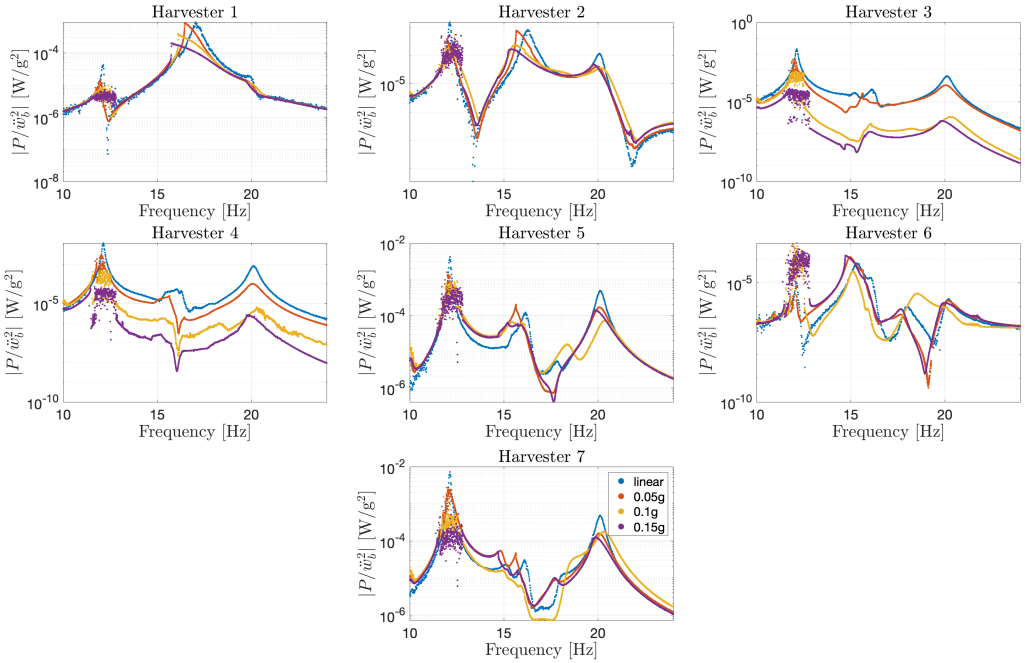

(a)

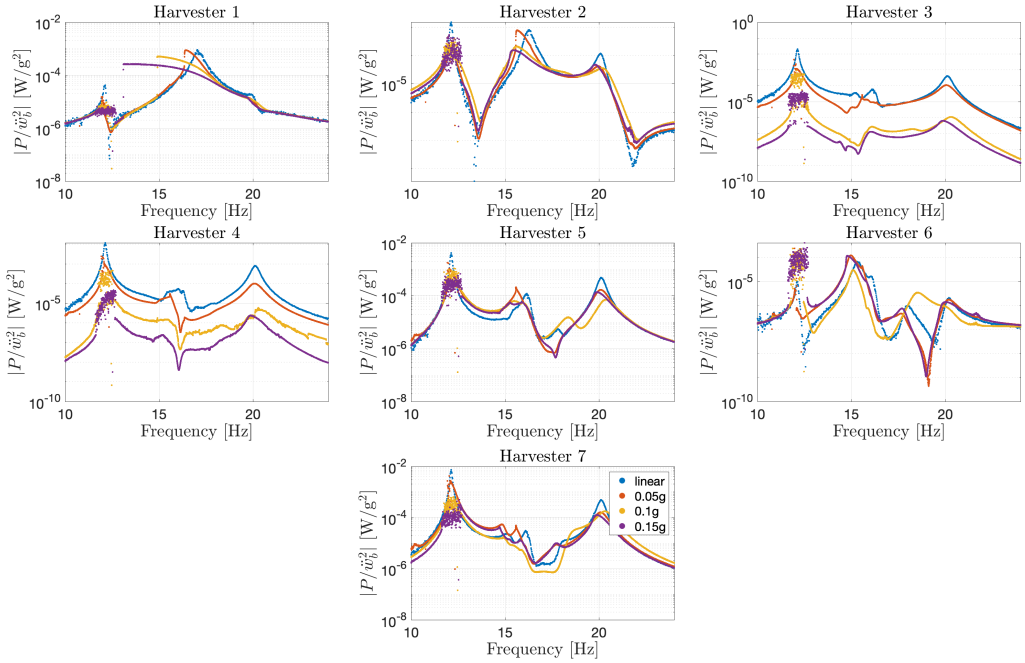

(b)

Figure 4.9: Experimentally obtained individual power output from each harvester at various acceleration levels at $R = 2.74M\Omega$ and $\omega_t/(2\pi) = 17$ Hz: (a) Up sweep. (b) Down sweep.

attenuation band, greater excitation amplitude also yields a wider power harvesting region for all loads.

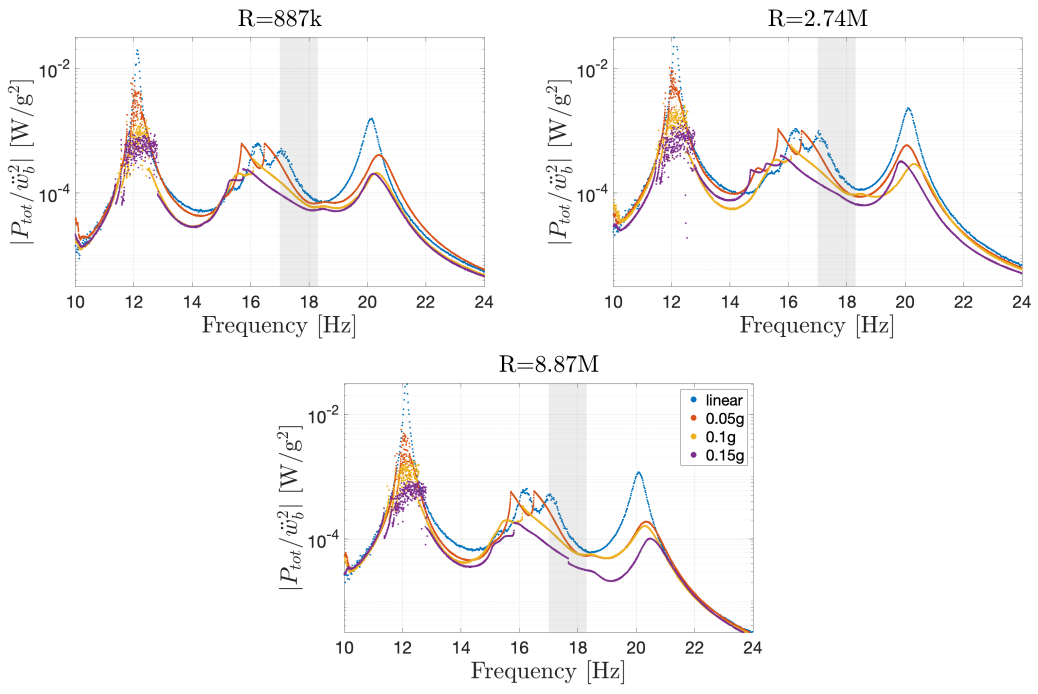

(a)

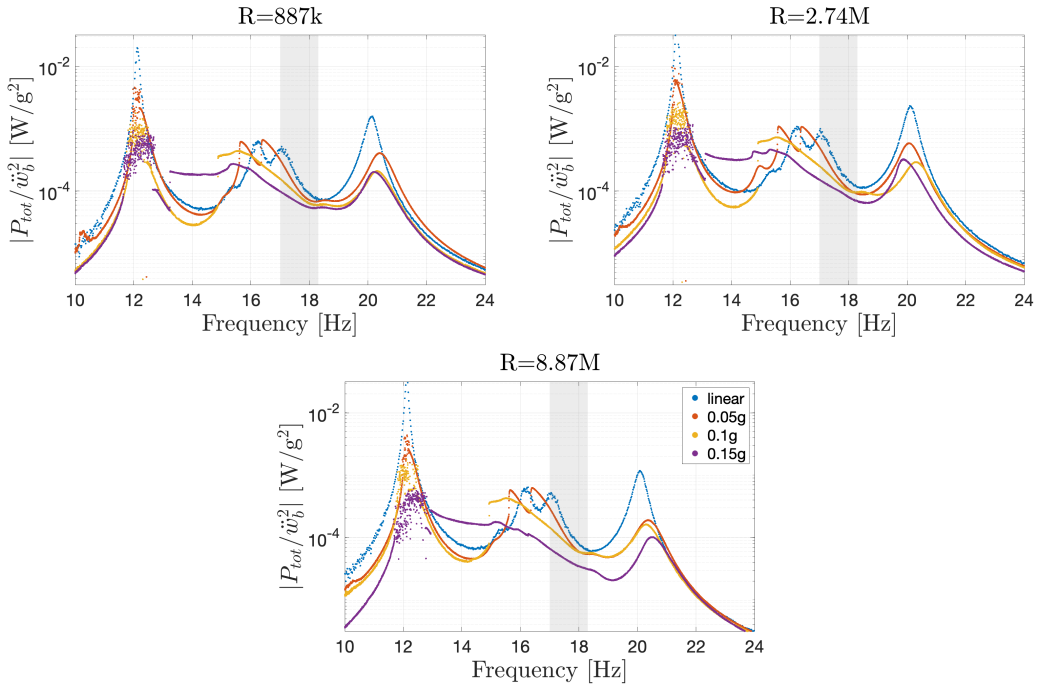

(b)

Figure 4.10: Experimentally obtained total power output of the complete nonlinear metastructure around the bandgap neighborhood displayed by the grey region: (a) Up sweep. (b) Down sweep.

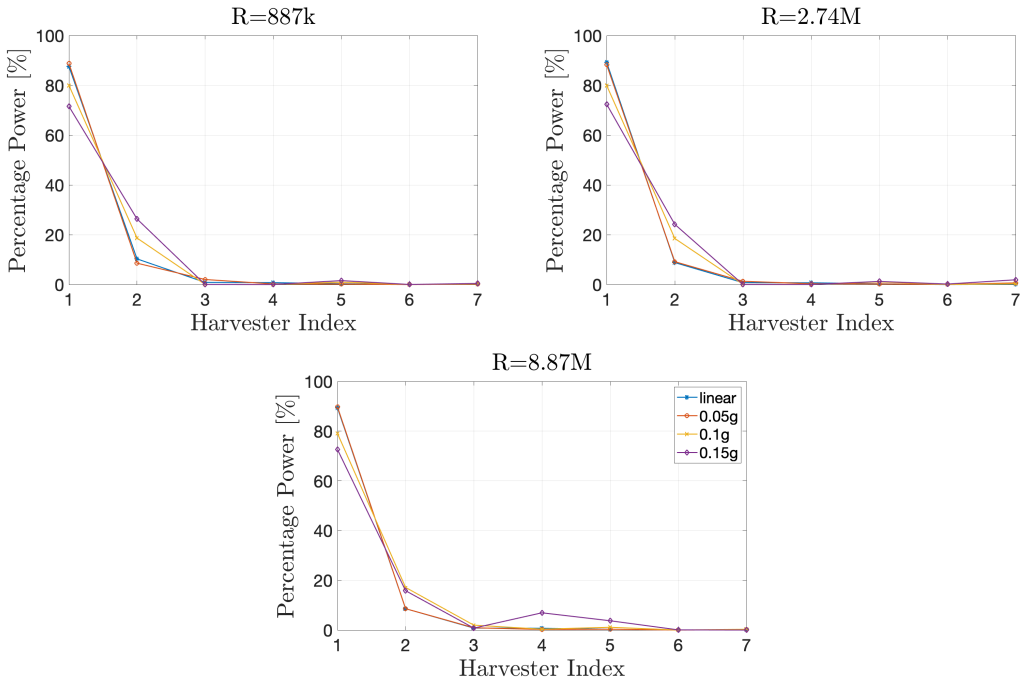

(a)

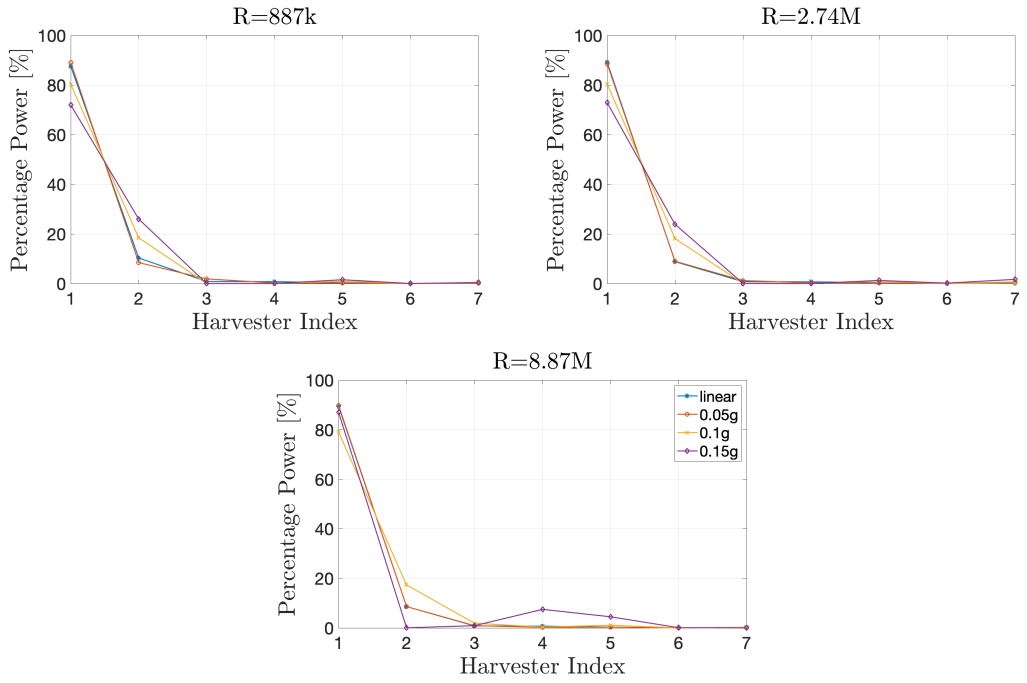

(b)

Figure 4.11: Percentage power contribution for the experiment as a function of harvester index at different excitation levels: (a) Up sweep. (b) Down sweep.

Each bistable harvester's contribution to total power can be seen as a percentage in Figure 4.11 at all load values for different excitation levels. As established in the previous section, the first harvester contributes most towards the total power and this decreases with increasing excitation (for $R = 2.74\,\mathrm{M}\Omega$, 88% for linear case and 72% at $0.15g$). However, moving towards the end of the beam, an increase in power output can be seen in other unit cells due to the broadband characteristic of bistable attachments. This trend increases with increasing g levels for example, for $R = 2.74\,\mathrm{M}\Omega$ at $0.15g$, second piezoelectric segment accounts for the maximum power contribution with 24% as compared to other cases for the same unit cell with minimum being 9% for the linear case. This is because of the nonlinear wideband characteristic of the resonators which spreads out the useful power output between piezoelectric elements due to an enhanced frequency range.

Overall, the experimental results verify the numerical simulations nicely with some discrepancies. These can be attributed to the fact that, first, the numerical model was devoid of the extrusions present in the actual beam and assumed it to be uniform. Secondly, stiffness for the springs were calculated using bistable equilibrium positions and post-buckled linear natural frequency of the attachments which made them rather simplified. Variation in the manual adjustment of magnets is also a case for slight difference in natural frequencies of the attachments. Adding to that, the asymmetry in clamping hardware directly corresponds to slightly asymmetric potential wells which invoke the inevitable quadratic nonlinearity, the effects of which can be studied in research like that done by He [74], Wang et al. [75], etc. Furthermore, the electromechanical coupling term was not fine tuned which caters to the small differences between numerical and experimental data.

4.4 Conclusion

The nonlinear metastructure brings forth opportunities to enable vibration attenuation and energy harvesting capabilities over a wider range of frequencies in comparison to its linear counterparts. This chapter reviews the governing equations for the nonlinear beam with

bistable attachments followed by corresponding numerical and experimental simulations. It shows that the bistability of attachments initiates intrawell softening and chaotic interwell oscillations which provide broadband frequency range for the respective bandgap. This enhanced frequency range not only widens the bandgap but also suppresses surrounding vibrational modes thereby increasing the total attenuating region. Simultaneously, it also allows to harvest power from these chaotic regions due to the nonlinear wideband behavior, and this useful power output region is not affected as we move along the beam from the clamped to free end. Furthermore, this thesis shows that these nonlinear systems are amplitude dependent and hence increasing the base excitation decreases the depth but broadens the corresponding attenuation band while also enhancing the power harvesting frequency range. Future research can be conducted on more asymmetric bistable attachments and other nonlinearities to study the effect of nonlinear dynamics on VEH capabilities.

CHAPTER 5
CONCLUSIONS

Vibrational energy exists all around us which can be harmful but can also provide opportunities for low-power electricity generation via energy harvesting. To this end, research has been conducted around the globe to not only attenuate the corresponding vibrations but also utilize the energy for our own benefit. This is currently a growing field and warrants a great amount of in-depth understanding to achieve the described goals. So far multiple ways have been developed to simultaneously work towards these. Various structures have been formed with designed properties called metastructures to research upon the benefits of vibration while simultaneously mitigating its harmful effects. Traditional vibration absorbers have been developed and used conventionally to attenuate structural vibrations. In addition, transducers such as piezoelectric patches have been utilized in order to extract the usefulness from these vibrations. These piezoelectric patches convert mechanical energy into usable electrical energy whereas resonators help to quantify these electrical voltage outputs and convert them to useful power for low-power appliances and sensors. Utilizing this opportunity, this thesis discusses multifunctional VEH catering to locally resonant (LR) metastructures. It starts with discussion on linear metastructures with focus on both mechanical and electromechanical metastructures where the difference lies in the type of resonators used to attenuate vibrations and harness power. Then the thesis moves on to more nonlinear metastructures where bistability of resonators accounts for its attenuating and harvesting capabilities at different load resistances. Initially an analytical framework is reviewed to establish governing equations for all kinds of metastructures. Then it presents numerical results followed by experimental validation of the said results to develop useful conclusions.

In case of mechanical LR metastructures, mechanical resonators are employed to atten-

uate vibrations around the resonant frequency of these resonators. Piezoelectric elements are used in the resonators for energy harvesting. It can be concluded from the analysis that most of the vibrational energy is localized near the base of the beam and maximum power output can be obtained immediately before the bandgap at the specified target frequency ratio after validation of the bandgap for the defined number of resonators. Moreover, as we move further away from the harvester nearest to the area of excitation, the corresponding power output decreases. The electromechanical case makes use of synthetic impedance circuits to attain the same result but unlike mechanical metastructures, using shunt circuitry to provide the electrical impedance responsible for bandgap formation in such structures. Hence, this type of metamaterial-based structure provides more advantage over conventional mechanical resonators as it not only gives freedom of tuning the bandgap, since it depends on the electrical impedance, but also eliminates the requirement of mass addition to the structure. Furthermore, it also allows for greater design flexibility as bandgap can be tuned according to the impedance of the synthetic shunt circuit and so can be used for more sensitive devices. The bandgap in an electromechanical LR metastructure varies with change in resistive loading. A decrease in the load resistance from OC to SC characteristics also reduces the depth and width of the bandgap until it fades away. Simultaneously, an opposing trend can be observed in useful power output where a transition towards SC conditions allows for an increase in power. This thesis details the existence of an optimal value of shunt loading where both vibration reduction and power harvesting can occur at the same time. This gives rise to a trade-off between vibration attenuation and useful power generation, where both can be targeted at optimal loading only.

The nonlinear metastructure with bistable attachments brings forth opportunities to obtain vibration attenuation and energy harvesting capabilities over a wider range of frequencies in comparison to its linear counterparts. It shows that the bistability of attachments initiates intrawell softening and chaotic interwell oscillations which provide broadband frequency range for the respective bandgap. This enhanced frequency range not only widens

the bandgap but also suppresses surrounding vibrational modes thereby increasing the total attenuating region. Simultaneously, it also allows for harvesting power from these chaotic frequency regions due to the nonlinear wideband behavior, and this useful power output region is not affected as we move along the beam from the clamped to free end. Furthermore, these nonlinear systems are amplitude dependent and hence increasing the base excitation decreases the depth but broadens the corresponding attenuation band while also enhancing the power harvesting frequency range. Future research can be conducted on more asymmetric bistable attachments and other nonlinearities to study the effect of nonlinear dynamics on VEH capabilities.

REFERENCES

[1] P. D. Frischmann, K. Mahata, and F. Würthner, "Powering the future of molecular artificial photosynthesis with light-harvesting metallosupramolecular dye assemblies," *Chem. Soc. Rev.*, vol. 42, pp. 1847–1870, 4 2013.

[2] G. Tiwari, R. Mishra, and S. Solanki, "Photovoltaic modules and their applications: A review on thermal modelling," *Applied Energy*, vol. 88, no. 7, pp. 2287–2304, 2011.

[3] A. A. Husain, W. Z. W. Hasan, S. Shafie, M. N. Hamidon, and S. S. Pandey, "A review of transparent solar photovoltaic technologies," *Renewable and Sustainable Energy Reviews*, vol. 94, pp. 779–791, 2018.

[4] Y. Chen, C. Pan, C. Lin, C. Hwang, and H. Chen, "Photovoltaic energy harvesting in indoor environments," in *2018 IEEE International Instrumentation and Measurement Technology Conference (I2MTC)*, 2018, pp. 1–5.

[5] A. Cuadras, M. Gasulla, and V. Ferrari, "Thermal energy harvesting through pyroelectricity," *Sensors and Actuators A: Physical*, vol. 158, no. 1, pp. 132–139, 2010.

[6] O. Ando Junior, A. Maran, and N. Henao, "A review of the development and applications of thermoelectric microgenerators for energy harvesting," *Renewable and Sustainable Energy Reviews*, vol. 91, pp. 376–393, 2018.

[7] R. Tian, C. Wan, N. Hayashi, T. Aoai, and K. Koumoto, "Wearable and flexible thermoelectrics for energy harvesting," *MRS Bulletin*, vol. 43, pp. 193–198, Mar. 2018.

[8] R. L. Harne and K. W. Wang, "A review of the recent research on vibration energy harvesting via bistable systems," *Smart Materials and Structures*, vol. 22, no. 2, p. 023 001, Jan. 2013.

[9] H. Wang, A. Jasim, and X. Chen, "Energy harvesting technologies in roadway and bridge for different applications – a comprehensive review," *Applied Energy*, vol. 212, pp. 1083–1094, 2018.

[10] P. L. Díez, I. Gabilondo, E. Alarcón, and F. Moll, "A comprehensive method to taxonomize mechanical energy harvesting technologies," in *2018 IEEE International Symposium on Circuits and Systems (ISCAS)*, 2018, pp. 1–5.

[11] F. Narita and M. Fox, "A review on piezoelectric, magnetostrictive, and magnetoelectric materials and device technologies for energy harvesting applications," *Advanced Engineering Materials*, vol. 20, p. 1 700 743, Nov. 2017.

[12] S. Priya and D. J. Inman, *Energy harvesting technologies*. Springer, 2009, vol. 21.

[13] N. Elvin and A. Erturk, *Advances in energy harvesting methods*. Springer Science & Business Media, 2013.

[14] M. T. Todaro, F. Guido, V. Mastronardi, D. Desmaele, G. Epifani, L. Algieri, and M. De Vittorio, "Piezoelectric mems vibrational energy harvesters: Advances and outlook," *Microelectronic Engineering*, vol. 183-184, pp. 23–36, 2017.

[15] C. A. Howells, "Piezoelectric energy harvesting," *Energy Conversion and Management*, vol. 50, no. 7, pp. 1847–1850, 2009.

[16] S. R. Anton and H. A. Sodano, "A review of power harvesting using piezoelectric materials (2003–2006)," *Smart materials and Structures*, vol. 16, no. 3, R1, 2007.

[17] M. Safaei, H. A. Sodano, and S. R. Anton, "A review of energy harvesting using piezoelectric materials: State-of-the-art a decade later (2008–2018)," *Smart Materials and Structures*, vol. 28, no. 11, p. 113 001, Oct. 2019.

[18] P. Glynne-Jones, M. Tudor, S. Beeby, and N. White, "An electromagnetic, vibration-powered generator for intelligent sensor systems," *Sensors and Actuators A: Physical*, vol. 110, no. 1, pp. 344–349, 2004, Selected Papers from Eurosensors XVI Prague, Czech Republic.

[19] C. Williams, C. Shearwood, M. Harradine, P. Mellor, T. Birch, and R. Yates, "Development of an electromagnetic micro-generator," *IEE Proceedings - Circuits, Devices and Systems*, vol. 148, 337–342(5), 6 Dec. 2001.

[20] L. G. W. Tvedt, D. S. Nguyen, and E. Halvorsen, "Nonlinear behavior of an electrostatic energy harvester under wide- and narrowband excitation," *Journal of Microelectromechanical Systems*, vol. 19, no. 2, pp. 305–316, 2010.

[21] P. Mitcheson, P. Miao, B. Stark, E. Yeatman, A. Holmes, and T. Green, "Mems electrostatic micropower generator for low frequency operation," *Sensors and Actuators A: Physical*, vol. 115, no. 2, pp. 523–529, 2004, The 17th European Conference on Solid-State Transducers.

[22] S. Roundy and P. K. Wright, "A piezoelectric vibration based generator for wireless electronics," *Smart Materials and Structures*, vol. 13, no. 5, pp. 1131–1142, Aug. 2004.

[23] N. E. Dutoit and B. L. Wardle, "Performance of microfabricated piezoelectric vibration energy harvesters," *Integrated Ferroelectrics*, vol. 83, no. 1, pp. 13–32, 2006.

[24] A. Erturk and D. Inman, *Piezoelectric Energy Harvesting*. John Wiley & Sons, Ltd, 2011, ISBN: 9781119991151.

[25] K. A. Cook-Chennault, N. Thambi, and A. M. Sastry, "Powering MEMS portable devices—a review of non-regenerative and regenerative power supply systems with special emphasis on piezoelectric energy harvesting systems," *Smart Materials and Structures*, vol. 17, no. 4, p. 043 001, Jun. 2008.

[26] C. Sugino and A. Erturk, "Analysis of multifunctional piezoelectric metastructures for low-frequency bandgap formation and energy harvesting," *Journal of Physics D: Applied Physics*, vol. 51, no. 21, p. 215 103, May 2018.

[27] A. Erturk and D. Inman, "Broadband piezoelectric power generation on high-energy orbits of the bistable duffing oscillator with electromechanical coupling," *Journal of Sound and Vibration*, vol. 330, no. 10, pp. 2339–2353, 2011, Dynamics of Vibro-Impact Systems.

[28] A. F. Arrieta, P. Hagedorn, A. Erturk, and D. J. Inman, "A piezoelectric bistable plate for nonlinear broadband energy harvesting," *Applied Physics Letters*, vol. 97, no. 10, p. 104 102, 2010.

[29] Y. Shindo and F. Narita, "Dynamic bending/torsion and output power of s-shaped piezoelectric energy harvesters," *International Journal of Mechanics and Materials in Design*, vol. 10, pp. 305–311, Sep. 2014.

[30] J. Hoffmann and D. Inman, "A piezomagnetoelastic structure for broadband vibration energy harvesting," *Applied Physics Letters*, vol. 94, pp. 254 102–254 102, Jun. 2009.

[31] J. C. Park and J. Y. Park, "Asymmetric pzt bimorph cantilever for multi-dimensional ambient vibration harvesting," *Ceramics International*, vol. 39, S653–S657, 2013, The 8th Asian Meeting on Electroceramics (AMEC-8).

[32] H. Wu, L. Tang, Y. Yang, and C. K. Soh, "A novel two-degrees-of-freedom piezoelectric energy harvester," *Journal of Intelligent Material Systems and Structures*, vol. 24, no. 3, pp. 357–368, 2013.

[33] Z. Liu, X. Zhang, Y. Mao, Y. Y. Zhu, Z. Yang, C. T. Chan, and P. Sheng, "Locally resonant sonic materials," *Science*, vol. 289, no. 5485, pp. 1734–1736, 2000.

[34] C. Sugino, S. Leadenham, M. Ruzzene, and A. Erturk, "On the mechanism of bandgap formation in locally resonant finite elastic metamaterials," *Journal of Applied Physics*, vol. 120, no. 13, p. 134 501, 2016.

[35] R. Zhu, X. Liu, G. Hu, C. Sun, and G. Huang, "Negative refraction of elastic waves at the deep-subwavelength scale in a single-phase metamaterial," *Nat Commun*, vol. 5, Nov. 2014.

[36] N. Fang, D. Xi, J. Xu, M. Ambati, W. Srituravanich, C. Sun, and X. Zhang, "Ultrasonic metamaterials with negative modulus," *Nature materials*, vol. 5, pp. 452–6, Jul. 2006.

[37] "Energetic criterion of material vibration-fatigue failure," in *Proceedings of The 7th International Conference On Fracture (ICF7)*, K. SALAMA, K. RAVI-CHANDAR, D. TAPLIN, and P. R. RAO, Eds., Oxford: Pergamon, 1989, pp. 3853–3858, ISBN: 978-0-08-034341-9.

[38] V. P. Legeza, "Dynamics of Vibration Isolation System with a Ball Vibration Absorber," *International Applied Mechanics*, vol. 54, no. 5, pp. 584–593, Sep. 2018.

[39] G. H. Yoon, H. Choi, and H. So, "Development and optimization of a resonance-based mechanical dynamic absorber structure for multiple frequencies," *Journal of Low Frequency Noise, Vibration and Active Control*, vol. 0, no. 0, p. 1 461 348 419 855 533, 0.

[40] R. I. Wright and M. R. F. Kidner, "Vibration absorbers: A review of applications in interior noise control of propeller aircraft," *Journal of Vibration and Control*, vol. 10, no. 8, pp. 1221–1237, 2004.

[41] A. D. Nashif, D. I. Jones, and J. P. Henderson, *Vibration damping*. John Wiley & Sons, 1985.

[42] D. I. Jones, *Handbook of viscoelastic vibration damping*. John Wiley & Sons, 2001.

[43] S. Behrens, A. J. Fleming, and S. O. R. Moheimani, "Passive vibration control via electromagnetic shunt damping," *IEEE/ASME Transactions on Mechatronics*, vol. 10, no. 1, pp. 118–122, 2005.

[44] "Damping of structural vibrations with piezoelectric materials and passive electrical networks," *Journal of Sound and Vibration*, vol. 146, no. 2, pp. 243–268, 1991.

[45] S.-y. Wu, "Method for multiple-mode shunt damping of structural vibration using a single PZT transducer," in *Smart Structures and Materials 1998: Passive Damping and Isolation*, L. P. Davis, Ed., International Society for Optics and Photonics, vol. 3327, SPIE, 1998, pp. 159–168.

[46] J. J. Hollkamp, "Multimodal passive vibration suppression with piezoelectric materials and resonant shunts," *Journal of Intelligent Material Systems and Structures*, vol. 5, no. 1, pp. 49–57, 1994.

[47] A. J. Fleming, S. Behrens, and S. O. Reza Moheimani, "Optimization and implementation of multimode piezoelectric shunt damping systems," *IEEE/ASME Transactions on Mechatronics*, vol. 7, no. 1, pp. 87–94, 2002.

[48] B. Yan, H. Ma, L. Zhang, W. Zheng, K. Wang, and C. Wu, "A bistable vibration isolator with nonlinear electromagnetic shunt damping," *Mechanical Systems and Signal Processing*, vol. 136, p. 106 504, 2020.

[49] L. R. Corr and W. W. Clark, "Comparison of low-frequency piezoelectric switching shunt techniques for structural damping," *Smart Materials and Structures*, vol. 11, no. 3, pp. 370–376, May 2002.

[50] M. F. Daqaq, R. Masana, A. Erturk, and D. Dane Quinn, "On the Role of Nonlinearities in Vibratory Energy Harvesting: A Critical Review and Discussion," *Applied Mechanics Reviews*, vol. 66, no. 4, May 2014, 040801. eprint: https://asmedigitalcollection.asme.org/appliedmechanicsreviews/article-pdf/66/4/040801/6074385/amr_066_04_040801.pdf.

[51] A. Erturk, J. Hoffmann, and D. J. Inman, "A piezomagnetoelastic structure for broadband vibration energy harvesting," *Applied Physics Letters*, vol. 94, no. 25, p. 254 102, 2009.

[52] F. Cottone, H. Vocca, and L. Gammaitoni, "Nonlinear energy harvesting," *Phys. Rev. Lett.*, vol. 102, p. 080 601, 8 Feb. 2009.

[53] S. C. Stanton, C. C. McGehee, and B. P. Mann, "Nonlinear dynamics for broadband energy harvesting: Investigation of a bistable piezoelectric inertial generator," *Physica D: Nonlinear Phenomena*, vol. 239, no. 10, pp. 640–653, 2010.

[54] D. R. Johnson, R. L. Harne, and K. W. Wang, "A Disturbance Cancellation Perspective on Vibration Control Using a Bistable Snap-Through Attachment," *Journal of Vibration and Acoustics*, vol. 136, no. 3, Mar. 2014, 031006. eprint: https://asmedigitalcollection.asme.org/vibrationacoustics/article-pdf/136/3/031006/6340825/vib_136_03_031006.pdf.

[55] F. Romeo, G. Sigalov, L. A. Bergman, and A. F. Vakakis, "Dynamics of a Linear Oscillator Coupled to a Bistable Light Attachment: Numerical Study," *Journal of Computational and Nonlinear Dynamics*, vol. 10, no. 1, Sep. 2014, 011007. eprint: https://asmedigitalcollection.asme.org/computationalnonlinear/article-pdf/10/1/011007/6106104/cnd_010_01_011007.pdf.

[56] L. I. Manevitch, G. Sigalov, F. Romeo, L. A. Bergman, and A. Vakakis, "Dynamics of a Linear Oscillator Coupled to a Bistable Light Attachment: Analytical Study," *Journal of Applied Mechanics*, vol. 81, no. 4, Sep. 2013, 041011. eprint: https:

//asmedigitalcollection.asme.org/appliedmechanics/article-pdf/81/4/041011/6079482/jam_081_04_041011.pdf.

[57] K. Yang, R. L. Harne, K. W. Wang, and H. Huang, "Investigation of a bistable dual-stage vibration isolator under harmonic excitation," *Smart Materials and Structures*, vol. 23, no. 4, p. 045 033, Mar. 2014.

[58] H. Ding and L.-Q. Chen, "Designs, analysis, and applications of nonlinear energy sinks," *Nonlinear Dynamics*, vol. 100, Jun. 2020.

[59] B. Lazarov and J. Jensen, "Low-frequency band gaps in chains with attached non-linear oscillators," *International Journal of Non-Linear Mechanics*, vol. 42, no. 10, pp. 1186–1193, 2007.

[60] A. Banerjee, R. Das, and E. Calius, "Waves in structured mediums or metamaterials: A review," *Archives of Computational Methods in Engineering*, vol. 26, May 2018.

[61] *The Effects of Cubic Stiffness Nonlinearity on the Attenuation Bandwidth of 1D Elasto-Dynamic Metamaterials*, vol. Volume 13: Acoustics, Vibration, and Wave Propagation, ASME International Mechanical Engineering Congress and Exposition, V013T01A020, Nov. 2016.

[62] A. Casalotti, S. El-Borgi, and W. Lacarbonara, "Metamaterial beam with embedded nonlinear vibration absorbers," *International Journal of Non-Linear Mechanics*, vol. 98, Oct. 2017.

[63] Y. Xia, M. Ruzzene, and A. Erturk, "Bistable attachments for wideband nonlinear vibration attenuation in a metamaterial beam," *Nonlinear Dynamics*, vol. 102, pp. 1–12, Nov. 2020.

[64] ——, "Dramatic bandwidth enhancement in nonlinear metastructures via bistable attachments," *Applied Physics Letters*, vol. 114, no. 9, p. 093 501, 2019.

[65] S. Chiacchiari, F. Romeo, D. Mcfarland, L. Bergman, and A. Vakakis, "Vibration energy harvesting from impulsive excitations via a bistable nonlinear attachment," *International Journal of Non-Linear Mechanics*, vol. 94, Apr. 2017.

[66] P. Dorin, J. Kim, and K. W. Wang, "Vibration energy harvesting system with coupled bistable modules," in *Active and Passive Smart Structures and Integrated Systems XIII*, A. Erturk, Ed., International Society for Optics and Photonics, vol. 10967, SPIE, 2019, pp. 81–94.

[67] F. Romeo, L. I. Manevitch, L. A. Bergman, and A. Vakakis, "Transient and chaotic low-energy transfers in a system with bistable nonlinearity," *Chaos: An Interdisciplinary Journal of Nonlinear Science*, vol. 25, no. 5, p. 053 109, 2015.

[68] R. L. Harne, M. Thota, and K. W. Wang, "Bistable energy harvesting enhancement with an auxiliary linear oscillator," *Smart Materials and Structures*, vol. 22, no. 12, p. 125 028, Nov. 2013.

[69] C. Sugino, S. Leadenham, M. Ruzzene, and A. Erturk, "An investigation of electroelastic bandgap formation in locally resonant piezoelectric metastructures," *Smart Materials and Structures*, vol. 26, no. 5, p. 055 029, Apr. 2017.

[70] L. Meirovitch, *Principles and Techniques of Vibrations*, ser. Prentice Hall International Editions Series. Prentice Hall, 1997, ISBN: 9780132704304.

[71] C. Sugino, Y. Xia, S. Leadenham, M. Ruzzene, and A. Erturk, "A general theory for bandgap estimation in locally resonant metastructures," *Journal of Sound and Vibration*, vol. 406, pp. 104–123, 2017.

[72] A. Erturk and D. Inman, "A distributed parameter electromechanical model for cantilevered piezoelectric energy harvesters," *Journal of Vibration and Acoustics*, vol. 130, p. 041 002, 2008.

[73] C. Sugino, M. Ruzzene, and A. Erturk, "Digitally programmable resonant elastic metamaterials," *Phys. Rev. Applied*, vol. 13, p. 061 001, 6 Jun. 2020.

[74] Q. He and M. Daqaq, "Influence of potential function asymmetries on the performance of nonlinear energy harvesters under white noise," *Journal of Sound and Vibration*, vol. 333, pp. 3479–3489, Jul. 2014.

[75] W. Wang, J. Cao, C. Bowen, D. Inman, and J. Lin, "Performance enhancement of nonlinear asymmetric bistable energy harvesting from harmonic, random and human motion excitations," *Applied Physics Letters*, vol. 112, p. 213 903, May 2018.